Cell Reports

Article

The transcription factor BCL11A defines distinct subsets of midbrain dopaminergic neurons

Graphical abstract

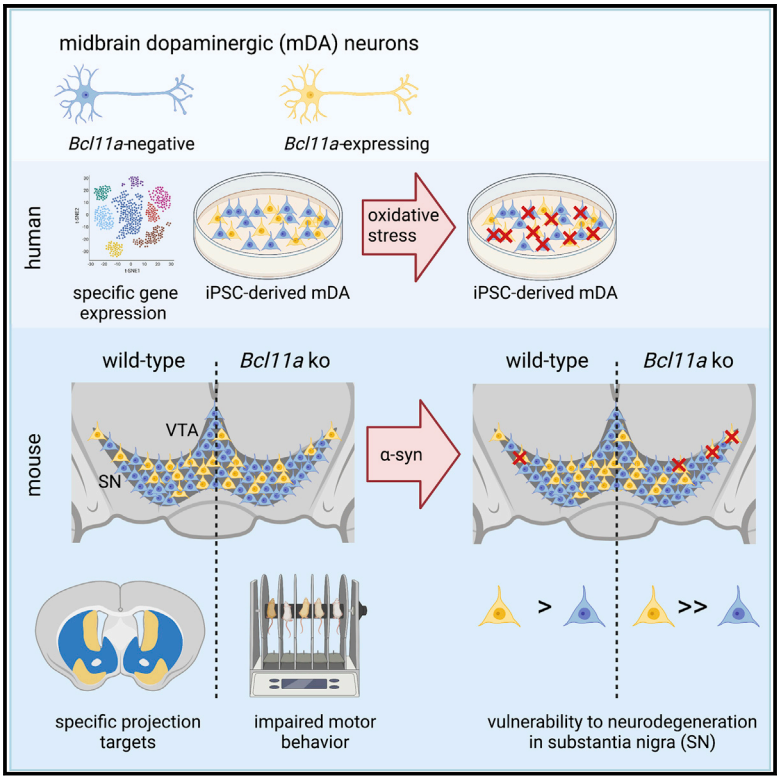

Highlights

- Bcl11a is expressed in a subset of murine and human dopaminergic neurons
- Bcl11a^{+} dopaminergic neurons form a highly specific subcircuit in mouse
- Bcl11a^{+} substantia nigra neurons are particularly vulnerable to neurodegeneration
- Bcl11a inactivation increases vulnerability and impairs motor behavior in mice

Authors

Marianna Tolve, Ayse Ulusoy, Nikolaos Patikas, ..., Stephan L. Baader, Donato A. Di Monte, Sandra Blaess

Correspondence

sblaess@uni-bonn.de

In brief

Little is known about the molecular mechanisms that establish diversity in the dopaminergic system. Tolve et al. show that the transcription factor BCL11A defines dopaminergic subpopulations with distinct projection targets and susceptibility to neurodegeneration and is required for the establishment and maintenance of normal function of this subset.

Tolve et al., 2021, Cell Reports *36*, 109697
September 14, 2021
https://doi.org/10.1016/j.celrep.2021.109697

CellPress

Cell Reports

CellPress
OPEN ACCESS

Article

The transcription factor BCL11A defines distinct subsets of midbrain dopaminergic neurons

Marianna Tolve,[1] Ayse Ulusoy,[2] Nikolaos Patikas,[3] K. Ushna S. Islam,[1] Gabriela O. Bodea,[1,10,11] Ece Öztürk,[1] Bianca Broske,[1] Astrid Mentani,[1] Antonia Wagener,[1] Karen M.J. van Loo,[4,12] Stefan Britsch,[5] Pengtao Liu,[6] Walid T. Khaled,[7,8] Emmanouil Metzakopian,[3] Stephan L. Baader,[9] Donato A. Di Monte,[2] and Sandra Blaess[1,13,*]

[1]Neurodevelopmental Genetics, Institute of Reconstructive Neurobiology, Medical Faculty, University of Bonn, 53127 Bonn, Germany
[2]German Center for Neurodegenerative Diseases (DZNE), 53127 Bonn, Germany
[3]UK Dementia Research Institute, Department of Clinical Neurosciences, Cambridge Biomedical Campus, University of Cambridge, Cambridge, CB2 0AH, UK
[4]Section for Translational Epilepsy Research, Department of Neuropathology, Medical Faculty, University of Bonn, 53127 Bonn, Germany
[5]Institute of Molecular and Cellular Anatomy, Ulm University, 89081 Ulm, Germany
[6]School of Biomedical Sciences, Li Ka Shing Faculty of Medicine, The University of Hong Kong, Hong Kong, China
[7]Department of Pharmacology, University of Cambridge, Cambridge, CB 21PD, UK
[8]Wellcome-MRC Cambridge Stem Cell Institute, Cambridge, CB2 0AW, UK
[9]Institute of Anatomy, Anatomy and Cell Biology, Medical Faculty, University of Bonn, 53115 Bonn, Germany
[10]Queensland Brain Institute, University of Queensland, Brisbane, Queensland, 4072, Australia
[11]Mater Research Institute-University of Queensland, TRI Building, Brisbane, Queensland, 4102, Australia
[12]Department of Epileptology, Neurology, RWTH Aachen University, 52074 Aachen, Germany
[13]Lead contact
*Correspondence: sblaess@uni-bonn.de
https://doi.org/10.1016/j.celrep.2021.109697

SUMMARY

Midbrain dopaminergic (mDA) neurons are diverse in their projection targets, effect on behavior, and susceptibility to neurodegeneration. Little is known about the molecular mechanisms establishing this diversity during development. We show that the transcription factor BCL11A is expressed in a subset of mDA neurons in the developing and adult murine brain and in a subpopulation of pluripotent-stem-cell-derived human mDA neurons. By combining intersectional labeling and viral-mediated tracing, we demonstrate that *Bcl11a*-expressing mDA neurons form a highly specific subcircuit within the murine dopaminergic system. In the substantia nigra, the *Bcl11a*-expressing mDA subset is particularly vulnerable to neurodegeneration upon α-synuclein overexpression or oxidative stress. Inactivation of *Bcl11a* in murine mDA neurons increases this susceptibility further, alters the distribution of mDA neurons, and results in deficits in skilled motor behavior. In summary, BCL11A defines mDA subpopulations with highly distinctive characteristics and is required for establishing and maintaining their normal physiology.

INTRODUCTION

Midbrain dopaminergic (mDA) neurons are anatomically organized into the substantia nigra (SN), ventral tegmental area (VTA), and retro-rubral field (RRF). These anatomically defined areas contain subpopulations of mDA neurons that are characterized by distinct connectivity and distinct effects on behavior (Cox and Witten, 2019; Engelhard et al., 2019; Morales and Margolis, 2017). The SN consists of the pars compacta (SNc), containing most SN-mDA neurons; the pars lateralis (SNl); and the pars reticularis (SNr). SNl mDA neurons project to the tail of the striatum (TS) (Menegas et al., 2015). Medial SNc mDA neurons send their axons to the dorsomedial striatum (DMS), and projections of the lateral SNc target the dorsolateral striatum (DLS) (Lerner et al., 2015). mDA neurons in the VTA project to the nucleus accumbens (NAc), the olfactory tubercle (OT), prefrontal cortex (PFC), and amygdala. The VTA is also anatomically divided into smaller domains, but the relationship between the anatomical location of mDA cell bodies and their projection targets is less well defined (Morales and Margolis, 2017).

In addition to these anatomical mDA subgroups, mDA neurons have been classified based on their molecular profile. A comparison of the currently available single-cell gene expression studies led to the proposal that there are at least 7 molecularly defined mDA subgroups. These subgroups do not necessarily correspond to mDA populations distinct by anatomical location, projection target, and functional output (Poulin et al., 2020), and thus, it is not clear to what extent these different levels of diversity can be reduced to a common denominator to define mDA diversity. Because anatomical position, molecular profile, and

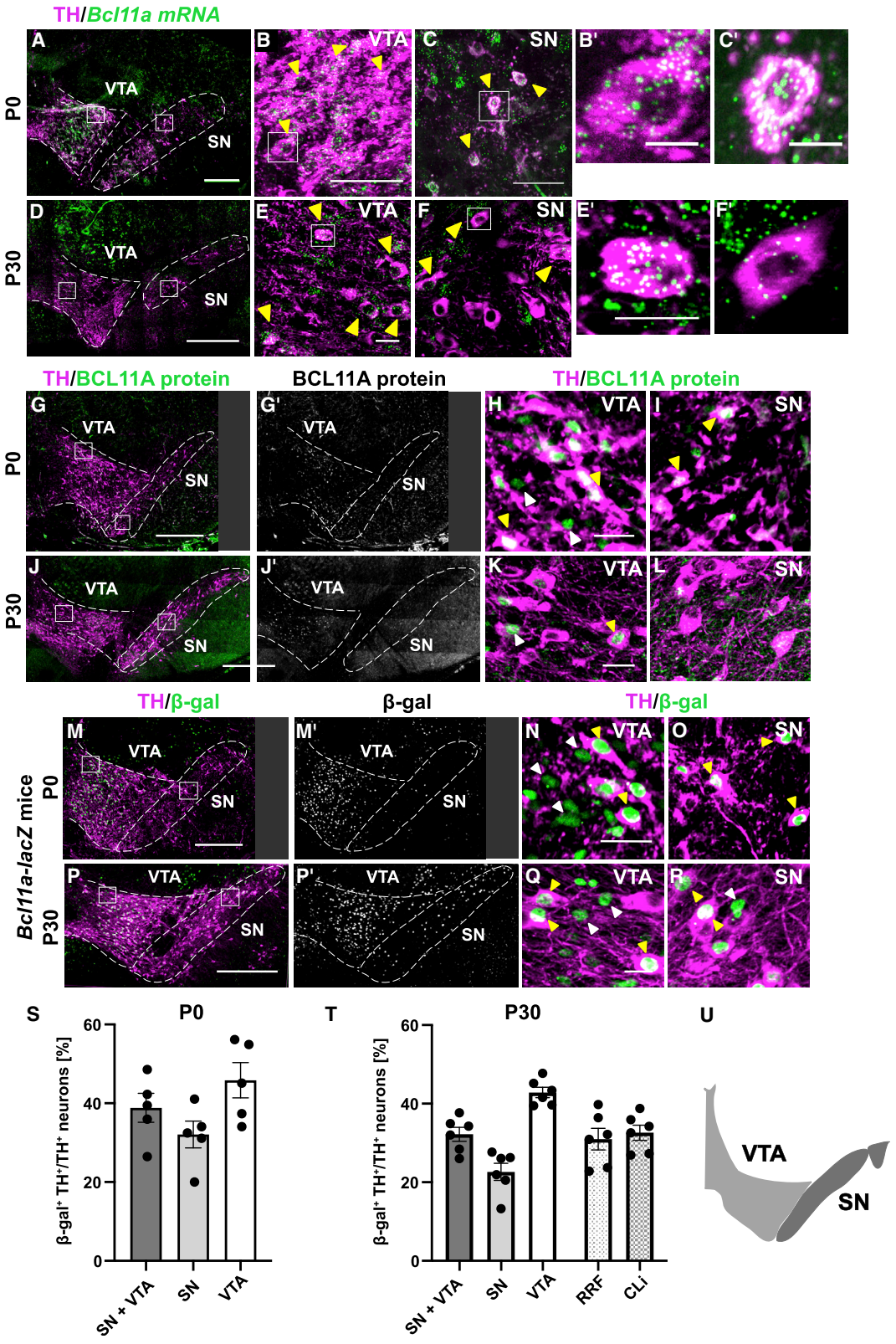

(legend on next page)

connectivity are largely determined during development, a better understanding of the developmental factors that determine mDA subpopulations could deliver important new insights on how to define mDA subpopulations.

mDA neurons in the SNc degenerate in Parkinson's disease (PD), leading to the cardinal motor symptoms of PD. mDA neurons in the VTA are much less affected by the neurodegeneration in PD and in various PD models in rodents, but even within the SNc, neurons are not homogeneous in their vulnerability: SNc-mDA neurons in the ventral tier appear to be more vulnerable than the ones in the dorsal tier (Surmeier et al., 2017). In mouse, ventral tier neurons express ALDH1A1 (Aldehyde Dehydrogenase 1 Family Member A1), whereas the less vulnerable subpopulation in the dorsal tier expresses the Calcium-binding protein Calbindin1 (CALB1) (Liu et al., 2014; Poulin et al., 2014; Thompson et al., 2005; Wu et al., 2019), suggesting that the susceptibility to neurodegeneration in mDA subgroups could be genetically and developmentally pre-determined.

Because transcription factors are key regulators of cell specification programs, we set out to identify transcription factors that are expressed in subpopulations of mDA neurons in the developing and adult brain. We discovered that the C2H2 zinc finger transcription factor BCL11A (B cell CLL/lymphoma 11A) is expressed in a subpopulation of mDA neurons from embryogenesis to adulthood. BCL11A is a transcriptional repressor and a dedicated subunit of the mammalian SWI/SNF complex, which functions as an ATP-dependent chromatin remodeler (Kadoch et al., 2013; Simon et al., 2020). In mouse, BCL11A regulates neuronal fate determination during cortex and spinal cord development (Simon et al., 2020). In humans, *BCL11A* haploinsufficiency results in neurodevelopmental disorders characterized by developmental delay, intellectual disability, and behavioral problems (Basak et al., 2015; Dias et al., 2016; Fitzgerald et al., 2015; Peron et al., 2019; Soblet et al., 2018). Although these studies point to the importance of BCL11A in the development of the central nervous system (CNS), the function of BCL11A in the development and maintenance of the dopaminergic (DA) system has not yet been examined.

RESULTS

BCL11A is expressed in a subset of mDA neurons in the mouse brain

We initially identified *Bcl11a* as a potential mDA-subset marker based on the expression pattern available on the Allen Brain Atlas (Developing Mouse Brain). To examine whether BCL11A/*Bcl11a* is indeed expressed in a subpopulation of mDA neurons, we analyzed the expression of *Bcl11a* mRNA and BCL11A protein in combination with tyrosine hydroxylase (TH), the rate limiting enzyme in dopamine synthesis. In the neonatal and postnatal day 30 (P30) brain, *Bcl11a* mRNA was expressed in a subset of SN, VTA, RRF, and caudal linear nucleus (CLi) neurons. In the SN, *Bcl11a*-expressing mDA neurons were predominantly localized to the SNl and the dorsal SNc. Within the VTA, *Bcl11a*-positive neurons were found primarily in the lateral VTA (Figures 1A–1F; data not shown). The distribution of neurons positive for BCL11A protein and TH was comparable to the distribution of *Bcl11a*/TH-positive neurons in the neonatal brain and in the VTA of P30 brains (Figures 1G–1L). However, we could not detect the BCL11A protein in mDA neurons in the SN at P30 (Figures 1J and 1L). *Bcl11a* mRNA is expressed at lower levels in SN- than in VTA-mDA neurons at P30 (Figures 1E and 1F), indicating that SN-mDA neurons may express the BCL11A protein at low levels that are undetectable with the anti-BCL11A antibody used in our study.

Next, we analyzed the distribution of *Bcl11a*-expressing cells by using $Bcl11a^{lacZ}$ mice. In this mouse line, the *lacZ* allele is knocked into the endogenous *Bcl11a* locus and β-gal expression is restricted to cells that express *Bcl11a* (Dias et al., 2016). Indeed, the distribution of β-gal-positive mDA neurons in neonatal and adult brain was comparable to the one of mDA neurons expressing *Bcl11a* mRNA (Figures 1A–1F and 1M–1R; Figure S1). Double labeling for β-gal and the BCL11A protein showed that the expression pattern of β-gal and BCL11A was largely overlapping in the VTA and in the cerebral cortex, indicating that β-gal reliably marks BCL11A-expressing neurons (Figures S2A–S2D). Quantification of β-gal and TH double-positive cells in VTA, SN, RRF, and CLi of neonatal and P30 *Bcl11a-lacZ* mice demonstrated that about one-third of mDA neurons express *Bcl11a* (Figures 1S and 1T; Figure S1G). Additionally, non-mDA neurons expressing β-gal were present medial to the VTA, dorsal to the SN, and within the VTA and SN area (Figures 1M and 1P; Figure S1).

An analysis of the developmental time course of BCL11A expression showed that BCL11A was first expressed in the ventral midbrain at embryonic day 12.5 (E12.5). At E12.5 and E13.5, BCL11A was mainly localized in the area just below the mDA progenitor domain and in a few differentiated TH-expressing mDA neurons. At E14.5 and E15.5, expression was found in a larger subset of mDA neurons in the forming SN and VTA (Figures S2E–S2I; data not shown).

Figure 1. BCL11A is expressed in a subset of mDA neurons

(A–F′) Immunostaining for TH and multiplex fluorescent *in situ* hybridization for *Bcl11a* mRNA on postnatal day 0 (P0) (A–C′) and P30 (D–F′) coronal sections. (B, C, E, and F) Higher magnification of the boxed areas in (A) and (D). (B′, C′, E′, and F′) Higher magnification of the boxed area in (B), (C), (E), and (F). SN-mDA neurons express lower levels of *Bcl11a* mRNA than VTA-mDA neurons, as evident by the density of fluorescent dots in the TH-positive cell.

(G–L) Immunostaining for BCL11A and TH on P0 (G–I) and P30 (J–L) coronal sections. (H, I, K, and L) Higher magnification of the boxed area in (G) and (J). Immunostaining for BCL11A failed to detect the protein in the SN at P30.

(M–R) Immunostaining for β-gal and TH on coronal sections of P0 (M–O) and P30 (P–R) *Bcl11a-lacZ* mice. (N, O, Q, and R) Higher magnification of the boxed areas in (M) and (P). Yellow arrowheads, cells double positive for TH and BCL11A/*Bcl11a*/β-gal; white arrowheads, cells that express BCL11A/*Bcl11a*/β-gal but are TH-negative.

(S and T) Percentage of β-gal-positive TH-expressing neurons in *Bcl11a-lacZ* mice at P0 (S; n = 5 mice) and P30 (T; n = 6 mice).

(U) Schematic of the SNl, SNc, and VTA level shown in (A)–(R). Error bars indicate mean ± SEM. Scale bars: 200 μm (A, G, G′, M, and M′), 500 μm (D, J, J′, P, and P′), 25 μm (B, C, E, E′, F, F′, H, I, K, L, N, O, Q, and R), and 10 μm (B′ and C′). See also Figures S1 and S2.

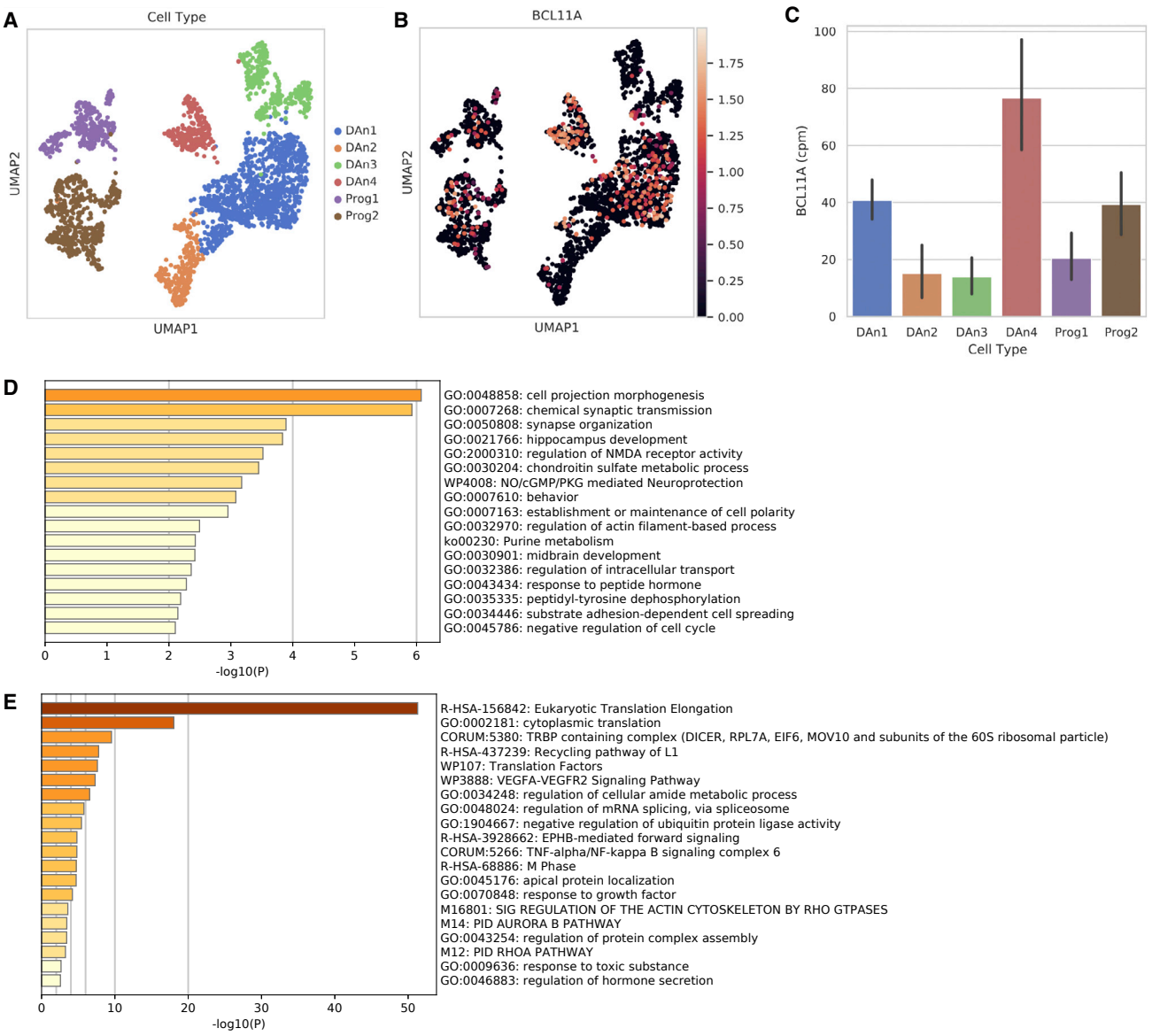

Figure 2. *BCL11A*-expressing hiPSC-derived mDA neurons show a distinct gene expression profile

(A and B) Low-dimension uniform manifold approximation and projection (UMAP) of single-cell transcriptomes. Culture of 2,648 hiPSC-derived human mDA neurons annotated by cell type (as in Fernandes et al., 2020) (A) and normalized for *BCL11A* expression (B).

(C) *BCL11A* expression levels (counts per million) detected in single cells aggregated by cell type. Error bars indicate 95% confidence intervals.

(D and E) Gene set enrichment analysis of the top 100 upregulated genes in *BCL11A*-positive DAn1 (D) or *BCL11A*-positive DAn4 (E) cells sorted according to statistical significance. See also Tables S1 and S2. For subtype characterization in mouse see Figure S3.

BCL11A-expressing human-stem-cell-derived mDA neurons show a distinct gene expression profile

To examine whether *BCL11A* is expressed in human mDA neurons, we analyzed data obtained from droplet-based single-cell RNA sequencing (scRNA-seq) of human induced pluripotent stem cell (hiPSC)-derived mDA neurons. These cultures contain multiple neuronal subtypes, including SNc-like (DAn1) and VTA-like (DAn4) mDA neurons as well as progenitor cells (Prog1 and Prog2) and neurons with characteristics that do not fully recapitulate *in vivo* mDA neuronal types (DAn2 and DAn3) (Figure 2A; Fernandes et al., 2020). DAn4 neurons were characterized by the combined expression of *CALB1*, *MARCK5*, and *NEFM*. DAn1 neurons were defined by the expression of *TH*, *NR4A2*, *FOXA2*, *LMX1A*, *DDC*, and *LMO3* and the absence of serotonergic markers (*TPH1*). In these cultures, *BCL11A* single-cell detection rates suggested some cell-type specificity with the most prominent expression in DAn4 neurons followed by expression in DAn1 neurons and a progenitor-like population (Prog2) (Figures 2A–2C).

We then investigated whether *BCL11A*-expressing mDA neurons show a distinct transcriptomic signature (Fernandes et al., 2020). Due to the high dropout rates of *BCL11A*, we were constrained to analyses between *BCL11A*-positive cells and *BCL11A*-negative cells in DAn1 (SNc-like) and DAn4 (VTA-like) cell types. A differential expression analysis of 162 positive and 1,107 negative DAn1 cells using a p value threshold of 0.05 highlighted 257 upregulated and 301 downregulated genes in the DAn1 population. *BCL11A* expression in DAn4 cells was found to be broader, with 81 positive and 276 negative cells with differential expression analysis identifying 167 upregulated and 70 downregulated genes. We then performed a gene set enrichment analysis of the 100 most significant upregulated genes in DAn1 and DAn4 *BCL11A*-positive cells. This analysis highlighted changes in cell projection morphogenesis, synaptic transmission, and synapse organization pathways for DAn1 *BCL11A*-expressing cells (Figure 2D; Table S1). In DAn4 *BCL11A*-positive cells, the analysis revealed prominent changes in translation (Figure 2E; Table S2). Taken together, *BCL11A* defines a distinct molecular signature within SNc-like (DAn1) and VTA-like (DAn4) hiPSC-derived mDA neurons. In DAn1 neurons, this gene expression profile suggests that neuronal maturation and function of *BCL11A*-expressing neurons may differ from *BCL11A*-negative DAn1 neurons.

Based on the differential expression analysis in hiPSC-derived mDA, *BCL11A*-expressing neurons do not fall into any of the previously characterized mDA subclasses (Poulin et al., 2020). To examine this in the mouse brain, we focused on the mDA subpopulations expressing ALDH1A1, CALB1, and SOX6 (SRY-Box Transcription Factor 6). ALDH1A1 is expressed in the ventral VTA, whereas CALB1 shows widespread expression in the VTA (Thompson et al., 2005; Wu et al., 2019). SOX6 expression is restricted to SN-mDA neurons and to neurons of the lateral VTA (Panman et al., 2014; Poulin et al., 2018). We performed triple immunostaining for β-gal, TH, and the respective subset marker (ALDH1A1, CALB1, or SOX6) in neonatal and P30 brain of *Bcl11a-lacZ* mice (Figures S3A–S3D). Quantification of triple-labeled mDA neurons (Figures S3E–S3H) showed that *Bcl11a*-expressing mDA neurons did not fully overlap with any of these markers, confirming that *Bcl11a*-positive mDA neurons do not clearly fall within one of these mDA subpopulations.

Bcl11a-expressing mDA neurons form a subcircuit in the DA system

If *Bcl11a*-expressing neurons indeed constitute a subset in the DA system, they should feature not only a specific molecular profile but also specific connectivity patterns. To examine whether the *Bcl11a*-expressing subclass of mDA neurons contributes to specific subcircuits in the mDA system, we specifically labeled cell bodies and projections of *Bcl11a*-expressing mDA neurons by using an intersectional genetic approach. This method is based on a reporter construct in which expression of a fluorescent protein is driven by a tetracycline response element (TRE) in a Cre-dependent manner (Madisen et al., 2015; Poulin et al., 2018). We first combined the intersectional reporter mouse line Ai82D (Madisen et al., 2015) with a Dat^{tTA} (tetracycline *trans*-activator driven by the *Dat* promoter) and a $Bcl11a^{CreER}$ mouse line (Chen et al., 2015; Poulin et al., 2018; Pensa et al., 2021; Figure 3A). Because BCL11A expression is already restricted to mDA subsets during embryogenesis (Figures S2F–S2I), CreER was activated by administering tamoxifen to pregnant females at E15.5 (Figure 3B). Distribution of the recombined (EGFP+) mDA neurons was comparable to the distribution of β-gal-expressing cells in *Bcl11a-lacZ* mice (Figures 3C, S1, and S4). An analysis of EGFP-positive fibers showed that in target areas of VTA-mDA neurons (Morales and Margolis, 2017), *Bcl11a*-expressing mDA neurons strongly innervated the lateral septum and the OT and the ventral and lateral shell of the NAc, but not the medial shell or core (Figures 3D and 3E; data not shown). Hardly any EGFP-positive fibers were observed in the amygdala, habenula, or PFC (data not shown). Moreover, *Bcl11a*-expressing mDA neurons showed a highly specific projection pattern to the TS and the caudal DMS (Figures 3D and 3E), which are target areas of mDA neurons in the SNl and the medial SNc, respectively (Lerner et al., 2015; Menegas et al., 2015; Poulin et al., 2018). Within these SN target areas, the densest innervation originating from recombined mDA neurons was observed in the ventral TS. Innervation of the dorsolateral and rostral striatum was very sparse.

Next, we investigated the projections of mDA neurons that express *Bcl11a* in the adult brain (1) to clarify whether *Bcl11a* expression defines the same subset of mDA neurons in the embryonic and adult brain and (2) to clearly delineate the projection targets of *Bcl11a*-expressing neurons in the SN versus in the VTA. We introduced reporter constructs by injecting recombinant adeno-associated viruses (rAAVs) into the SN or VTA of adult animals. CreER was subsequently activated by the administration of tamoxifen to achieve recombination (Figures 4A and 4B; Figures S5A and S5B). We took both an intersectional approach, in which we introduced an intersectional reporter construct into $Bcl11a^{CreER}$, Dat^{tTA} mice (Figures 4A and 4B), and a non-intersectional approach in which we delivered a Cre-dependent reporter construct into $Bcl11a^{CreER}$ mice (Figures S5A and S5B). Labeling of *Bcl11a*-expressing mDA neurons in the SN was scarcer than that in the VTA (Figures 4C, 4D, 4F, and 4G; Figures S5C, S5D, S5G, and S5H), which is consistent with a lower percentage of *Bcl11a*-expressing mDA neurons in the SN than in the VTA (Figure 1T). The sparse labeling allowed us to visualize patches of innervation likely derived from single SN axons. These patches were restricted to the DMS and ventral TS, consistent with the findings obtained with the embryonically induced intersectional labeling (Figure 3D; Figures 4E and 4E'; Figures S5E and S5F'). Characterization of the VTA projection targets showed strong innervation of the OT and the ventral and lateral shell of the NAc (Figures 4F–4I; Figures S5G–S5K), consistent with the innervation pattern observed with the embryonic labeling (Figure 3). In some animals (n = 6/10) with sparse labeling of *Bcl11a*-expressing VTA-mDA neurons, the OT was innervated in a stripe-like pattern, suggesting that axons from single neurons might target specific domains within the OT (Figure S5I). In conclusion, these results show that expression of *Bcl11a* in embryogenesis and adulthood defines subsets of SN and VTA mDA neurons that form a highly specific subcircuit within the mDA system.

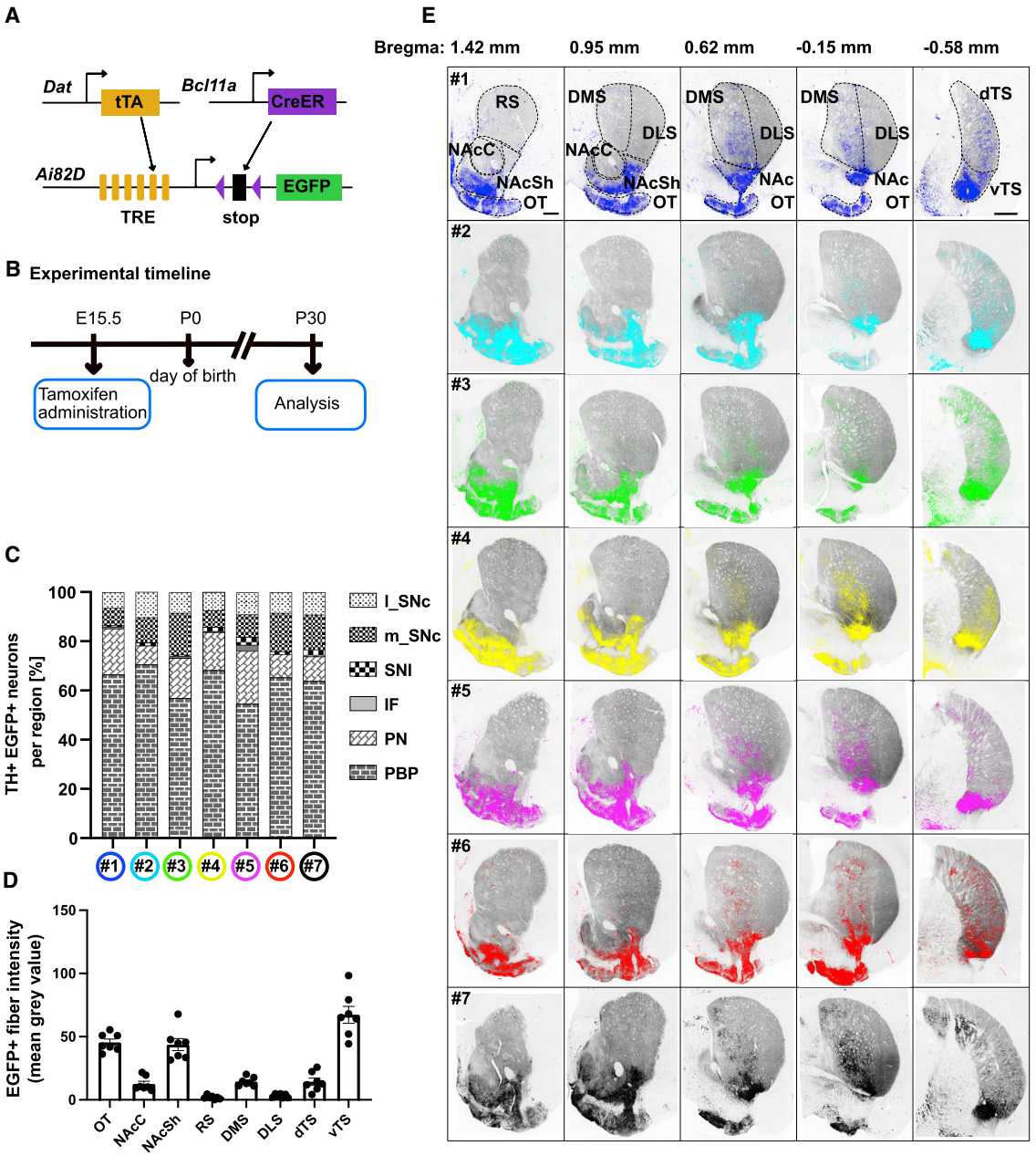

Figure 3. *Bcl11a*-expressing mDA neurons contribute projections to subcircuits of the dopaminergic system

(A) Intersectional fate mapping strategy to label *Bcl11a*-expressing mDA neurons and their projections. *Bcl11a*^{CreER} mice were used in combination with *Dat*^{tTA} mice and an intersectional reporter mouse line (*Ai82D*). EFGP is expressed only in cells positive for both CreER and tTa and only after CreER is activated by tamoxifen administration.

(B) Experimental timeline.

(C) Distribution of mDA neurons labeled with the intersectional fate mapping approach (EGFP+ and TH+) for individual mice (1–7). SN: l_SNc, lateral SNc; m_SNc, medial SNc; and SNl; VTA: IF, infundibular nucleus; PBP, parabrachial nucleus; and PN, paranigral nucleus (see Figure S1F). Colored circles are matched with the colors of the projection analysis in (E).

(D) Quantification of the density of mDA axons labeled with the intersectional fate mapping approach (EGFP+) in olfactory tubercle (OT), nucleus accumbens core (NacC), nucleus accumbens shell (NacSh), rostral striatum (RS), dorsomedial striatum (DMS), dorsolateral striatum (DLS), and ventral and dorsal tail of striatum (vTS and dTS, respectively). n = 7 mice. Error bars indicate mean ± SEM.

(E) Projections of mDA axons labeled with the intersectional fate mapping approach (EGFP+) in five rostrocaudal striatal coronal sections shown for individual mice (indicated by different colors, as in C). TH-positive fibers are shown in gray. Scale bars: 500 μm.

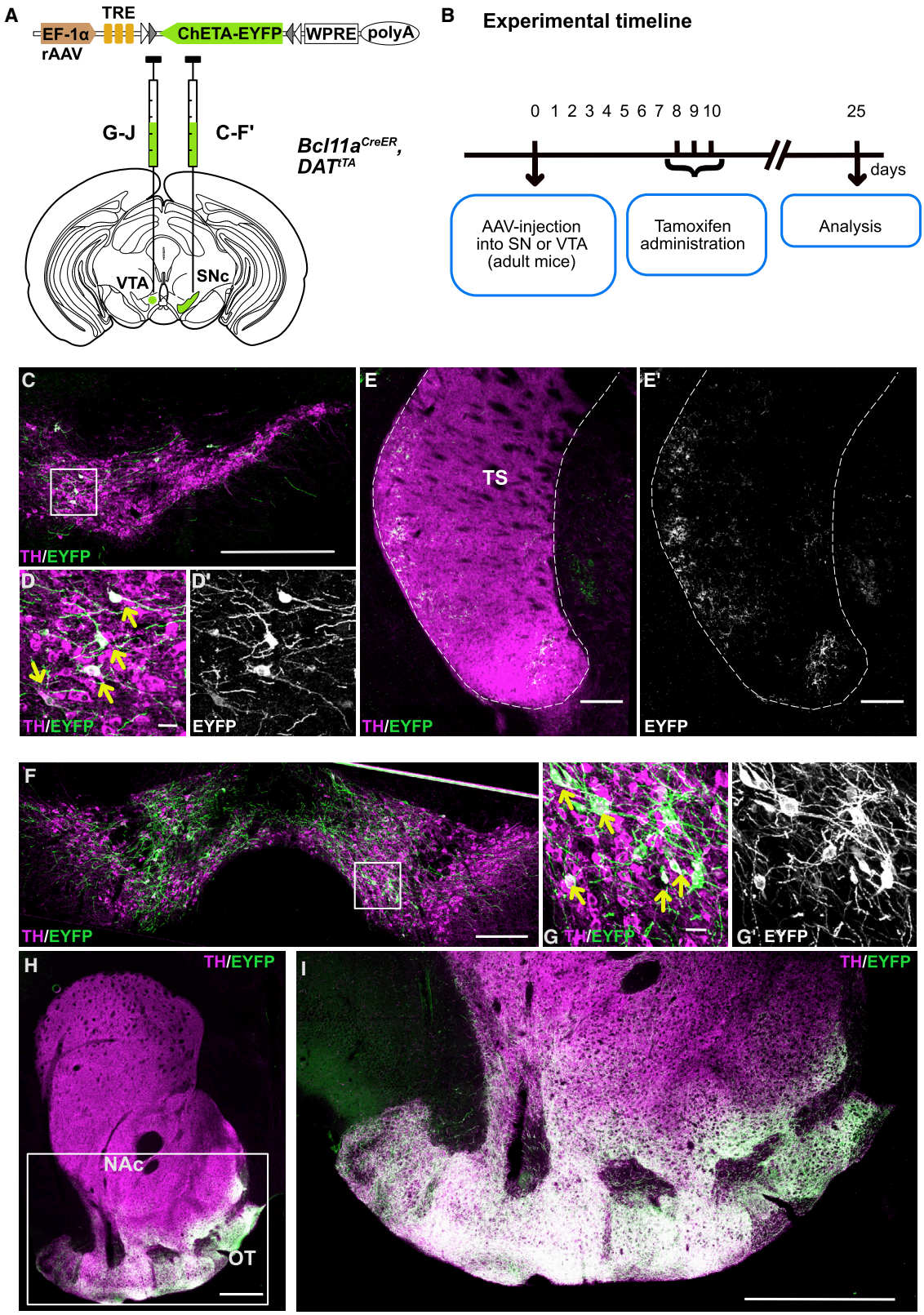

(legend on next page)

Conditional gene inactivation of *Bcl11a* in mDA neurons results in altered positioning of *Bcl11a*-mDA neurons

Because BCL11A is a transcription factor that has been shown to influence neuronal fate, neuronal morphology, and migration (Simon et al., 2020), we investigated whether BCL11A is necessary for establishing and/or maintaining *Bcl11a*-expressing mDA neurons. We generated a specific knockout for *Bcl11a* in mDA neurons by crossing *Bcl11a*^{flox} mice with *Dat*$^{IRES\text{-}Cre}$ mice (*Bcl11a* cko^{flox}; genotype: *Dat*$^{IRES\text{-}Cre/+}$, *Bcl11a*$^{flox/flox}$) (Bäckman et al., 2006; John et al., 2012). In a subset of mice, we introduced the *Bcl11a*^{lacZ} allele (a null allele; Dias et al., 2016) into the conditional knockout model (*Bcl11a* cko^{lacZ}; genotype: *Dat*$^{IRES\text{-}Cre/+}$, *Bcl11a*$^{flox/lacZ}$) (Figure 5A). In *Bcl11a* cko^{lacZ} mice, the *Bcl11a*-expressing mDA population expresses β-gal even after inactivation of *Bcl11a*, allowing us to analyze the effect of *Bcl11a* inactivation specifically in mDA neurons that would normally express BCL11A (termed *Bcl11a*-mDA neurons, β-gal and TH positive) (Figure 5B). We performed immunostaining and multiplex fluorescent *in situ* hybridization confirming that the BCL11A protein and *Bcl11a* mRNA expression were indeed absent in mDA neurons of *Bcl11a* cko^{flox} mice. As expected, BCL11A/*Bcl11a* was still expressed in non-mDA neurons in the midbrain and cerebral cortex (Figure S6).

The anatomical organization of the mDA area in *Bcl11a* conditional knockout (cko) (both in *Bcl11a* cko^{flox} and *Bcl11a* cko^{lacZ}) mice was comparable to that of controls (Figures 5C and 5D; data not shown), and the overall percentage of *Bcl11a*-mDA neurons (SN plus VTA) was not significantly changed between *Bcl11a* cko^{lacZ} and *Bcl11-lacZ* mice (Figures 5E and 5F). However, a detailed analysis by anatomical area and levels revealed alterations in the distribution of *Bcl11a*-mDA neurons in P30 *Bcl11a* cko^{lacZ} mice. The percentage of *Bcl11a*-mDA neurons was significantly increased in the CLi and significantly decreased at the most rostral level of the VTA (Figures 5F, S7A, and S7B). No significant rostral-to-caudal shift in the percentage of *Bcl11a*-mDA neurons could be detected in the SNc or SNl of *Bcl11a* cko^{lacZ} mice, but in the rostral SNc, *Bcl11a*-mDA were shifted from medial to lateral as compared to controls (Figures 5G, S7C, and S7D). These results indicate that the specific inactivation of *Bcl11a* in mDA neurons does not interfere with the generation or the survival of the *Bcl11a*-mDA neuronal population but that it results in altered positioning of *Bcl11a*-mDA neurons in the VTA and SNc.

If BCL11A is important for determining the localization of mDA neurons, it may also influence cell fate by regulating the expression of subset markers or the target specificity of *Bcl11a*-mDA projections. However, triple labeling for β-gal, TH, and CALB1 at P0 and P30; for β-gal, TH, and SOX6 at P0; and for β-gal, TH, and ALDH1A1 at P30 did not reveal a significant change in the number of *Bcl11a*-mDA neurons co-expressing these markers in *Bcl11a* cko^{lacZ} mice as compared to *Bcl11a-lacZ* mice (Figures S7E–S7J and S3). To assess the targeting of projections arising from *Bcl11a*-mDA neurons, we examined the density of TH innervation in control and *Bcl11a* cko mice in the ventral TS and the OT (the two areas with the highest innervation density from *Bcl11a*-mDA neurons) and in the dorsal striatum and the dorsal TS. We found no significant difference in the density of the TH innervation in any of these areas when comparing control and *Bcl11a* cko mice (Figures S7K–S7Q). These data suggest that the inactivation of *Bcl11a* has no overt effect on the anatomy of *Bcl11a*-mDA neuronal projections.

Inactivation of *Bcl11a* in mDA neurons results in skilled motor learning deficits

To investigate whether the specific inactivation of *Bcl11a* in mDA neurons leads to functional impairment in the DA system, we examined behaviors associated with VTA and/or SN function in *Bcl11a* cko and control mice. In the open field, distance moved was not altered in *Bcl11a* cko mice as compared to controls, indicating that spontaneous motor behavior was not affected in the mutant mice (Figure 6A). Decreased dopamine release from the VTA is associated with anxiety- and depressive-like behavior, which can be assessed by monitoring the activity in the center of an open field (Tye et al., 2013; El Yacoubi et al., 2003). *Bcl11a* cko mice did not show a change in the frequency of crossing into the center and time spent in center or border area in the open field, indicating that the *Bcl11a* cko mice did not have an increased level of anxiety or depressive behavior (Figures 6B and 6C). Next, we focused on tasks in which dopamine release from SN-mDA neurons is thought to play a prominent role. Dopamine release in the striatum is crucial for voluntary movement and motor skill learning (Cox and Witten, 2019; Dodson et al., 2016; Wu et al., 2019). Motor coordination and balance were examined by monitoring the ability of mice to cross a balance beam (Luong et al., 2011). We found no difference in the performance of *Bcl11a* cko mice and control mice in this task (Figure 6D). To examine whether motor skill learning is altered in *Bcl11a* cko mice, mice had to perform an accelerating rotarod test (Costa et al., 2004). In this task, control mice improved their performance over time, as reflected in a continuous increase in the time to fall over a 5-day training period. In contrast, *Bcl11a* cko mice did not show any improvement in their performance over time, indicating that they were not able to learn this skilled motor task within the trial period (Figure 6E). These results show that the specific inactivation of *Bcl11a* in mDA neurons results in deficits in skilled motor learning and suggest that *Bcl11a*-mDA neurons are functionally impaired in the absence of BCL11A.

Figure 4. *Bcl11a*-expressing mDA neurons of the VTA and SN show a specific innervation pattern of forebrain targets

(A) Injection of rAAV with an intersectional reporter construct into the SNc or VTA of *Bcl11a*$^{CreER/+}$;*Dat*$^{tTA/+}$ mice.

(B) Experimental timeline. Tamoxifen administration 8 days after rAAV injection results in expression of the reporter protein (EYFP) in *Bcl11a*-expressing mDA neurons.

(C–E′) Immunostaining for TH and EYFP in the SN (C–D′) and the tail of the striatum (TS) (E and E′).

(F–I) Immunostaining for TH and EYFP in the VTA (F–G′), striatum (H), and NAc and OT (I). Yellow arrows, neurons positive for TH and reporter protein. n = 2 mice for SN injections, n = 3 mice for VTA injections. Scale bars: 500 μm (C, F, and H), 250 μm (E and I), and 25 μm (D, D′, G, and G′). See also Figure S4.

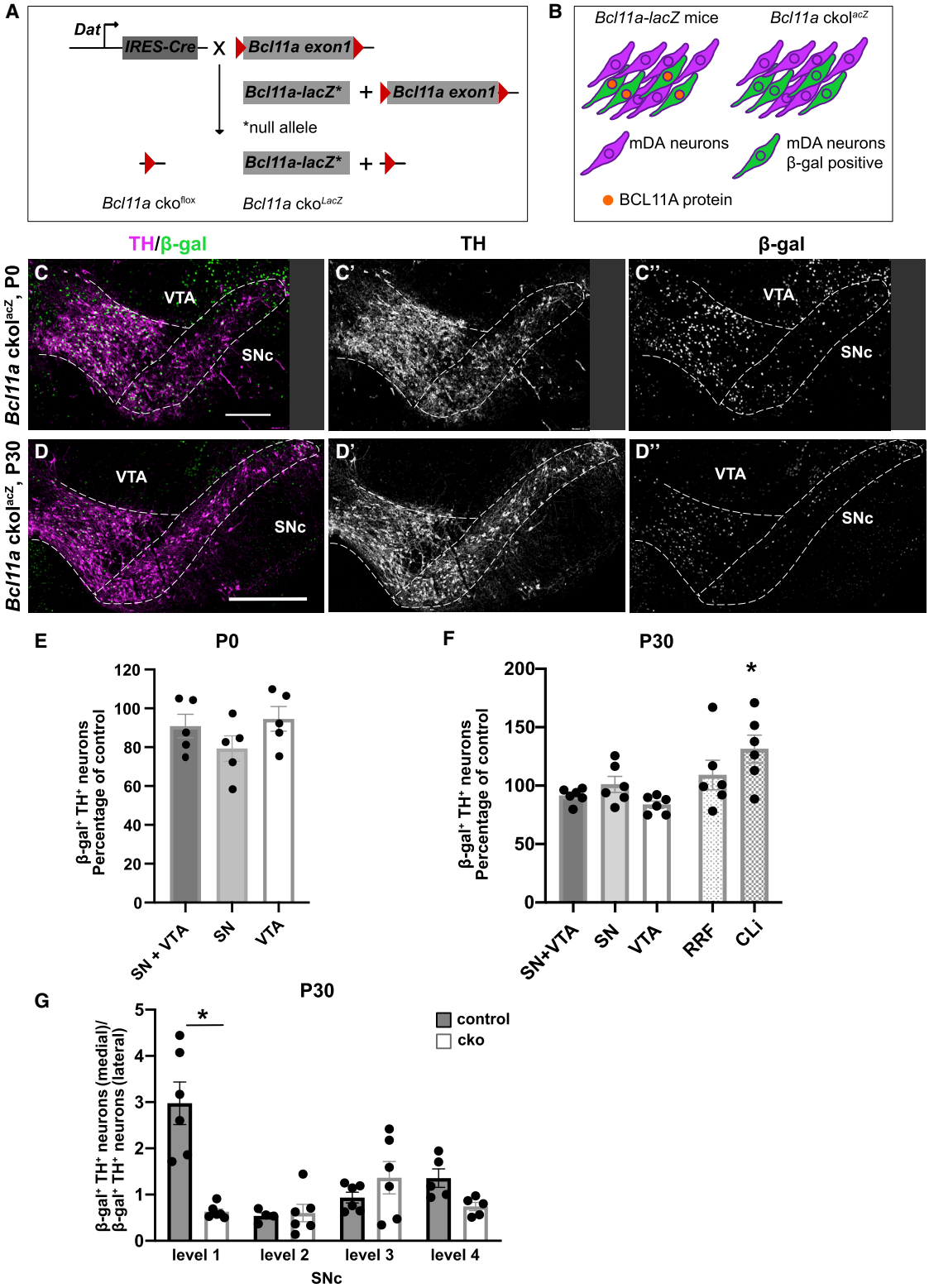

Figure 5. BCL11A is necessary for establishing the correct anatomical position of *Bcl11a*-expressing mDA neurons

(A) Conditional gene inactivation of *Bcl11a* in mDA neurons. *Bcl11a* cko mice were generated by crossing $Dat^{IRES\text{-}Cre}$ mice with $Bcl11a^{flox/flox}$ mice (genotype: $Dat^{RES\text{-}Cre/+}$, $Bcl11a^{flox/flox}$, termed *Bcl11a* cko^{flox}) or with $Bcl11a^{flox/lacZ}$ mice (genotype: $Dat^{IRES\text{-}Cre/+}$, $Bcl11a^{flox/lacZ}$, termed: *Bcl11a* cko^{lacZ}).

(B) In *Bcl11a* cko^{lacZ} mice, β-gal is a marker for *Bcl11a*-mDA neurons even after BCL11A expression is abolished.

(legend continued on next page)

BCL11A acts a neuroprotective factor in SNc-mDA neurons

The next set of experiments was aimed at elucidating the role of BCL11A in the context of neuronal challenges and neurodegenerative processes affecting mDA neurons in the SNc. The protein α-synuclein plays a key role in the pathogenesis of PD and other human neurodegenerative diseases (Goedert et al., 2013). Its overexpression in animal models is associated with PD-like pathology, including the degeneration of SNc-mDA neurons and accumulation of modified α-synuclein forms (Migdalska-Richards et al., 2017; Ulusoy and Di Monte, 2013). Adult control (n = 5) and *Bcl11a* cko (n = 5) mice were challenged with a single intraparenchymal injection of rAAVs carrying the DNA for human α-synuclein (Figure 7A). The unilateral injection targeted the right SNc where it caused robust overexpression of human α-synuclein within SNc-mDA neurons. Immunostaining against human α-synuclein showed no difference in overexpression between control and *Bcl11a* cko mice (Figure 7B).

Next, TH immunoreactivity was compared in the intact and injected side of the SNc in animals sacrificed 8 weeks after rAAV injection. Labeling was overtly less robust in the lesioned SNc of both control and *Bcl11a* cko mice, but the reduction in TH immunoreactivity appeared to be more pronounced in *Bcl11a* cko animals (Figure 7C). Stereological counts in the intact SNc were similar between control and *Bcl11a* cko mice and were therefore averaged together as normal values (5,988 ± 79.4 cells). Overexpression of α-synuclein caused a 15% reduction of TH^+ neurons in the lesioned SNc of control mice (5,086 ± 292.8 cells). This loss was significantly more pronounced (4,231 ± 208.2 cells) in *Bcl11a* cko mice (Figure 7D). The possibility that the decrease in neuronal counts after rAAV injection may reflect a downregulation of TH expression rather than actual cell degeneration was ruled out by counting the total number of Nissl-stained neurons. This number declined by 12% (from 9,185 ± 141.4 to 8,070 ± 525.6) and 27% (to 6,741 ± 326.1) in the lesioned SNc of control and *Bcl11a* cko mice, respectively (Figure 7E). Hyperphosphorylation is a consequence of intraneuronal α-synuclein accumulation and a marker of pathological changes in α-synuclein conformation and aggregation (Fujiwara et al., 2002; Migdalska-Richards et al., 2017). Midbrain sections from control and *Bcl11a* cko mice with rAAV-induced α-synuclein overexpression were immunostained with an antibody recognizing α-synuclein phosphorylated at Ser129 (p129-α-synuclein). Staining for p129-α-synuclein was virtually absent within SNc neurons on the intact side of the SNc (data not shown), whereas robust immunoreactivity characterized neurons in the injected SNc, consistent with an accumulation of pathological α-synuclein. The density of labeled neurons was decreased in the right SNc of *Bcl11a* cko mice as compared to control mice, likely reflecting the more pronounced nigral cell loss seen in *Bcl11a*-deficient animals (Figure 7F). Taken together, these findings reveal that vulnerability to α-synuclein toxicity is markedly enhanced in the absence of BCL11A and support the notion that BCL11A expression is associated with the transcription of genetic information involved in neuroprotective pathways.

The *Bcl11a*-expressing SNc-mDA neuronal subpopulation is highly vulnerable to toxic insults

Additional experiments using the same paradigm of rAAV-induced α-synuclein overexpression were carried out in *Bcl11a* cko^{lacZ} (n = 4) and *Bcl11a-lacZ* (genotype: *Bcl11a*$^{flox/lacZ}$) control (n = 5) mice. Like the results in *Bcl11a* cko animals without the lacZ allele, α-synuclein toxicity caused a more severe loss of TH-positive neurons in the SNc of *Bcl11a* cko^{lacZ} mice (from 5,954 ± 71.1 to 3,349 ± 193.3 cells) than that of *Bcl11a-lacZ* controls (from 5,954 to 5,041 ± 81.6 cells) (Figure 7G). In these experiments, confocal stereological counts were also able to distinguish the effects of α-synuclein overexpression on *Bcl11a*-mDA neurons in the SNc (TH^+ and β-gal^+) versus SNc-mDA neurons devoid of *Bcl11a* (TH^+ and β-gal^-). In *Bcl11a-lacZ* mice, 30% of β-gal^+ neurons (from 1,899 ± 70.8 to 1,332 ± 93.7 cells) degenerated because of α-synuclein overexpression, whereas no statistically significant changes were observed in the number of β-gal^- mDA cells between the lesioned and intact SNc (from 4,055 ± 118.8 to 3,709 ± 83.5 cells) (Figure 7H). These data indicate that *Bcl11a* expression characterizes a subpopulation of SNc-mDA neurons highly susceptible to α-synuclein-induced damage.

The number of β-gal^+ and β-gal^- neurons was then counted in the SNc of *Bcl11a* cko^{lacZ} animals. Results showed more dramatic toxic effects because α-synuclein toxicity killed almost 65% (from 1,899 to 664 ± 117.0 cells) and 34% (from 4,055 to 2,685 ± 91.4 cells) of β-gal^+ and β-gal^- cells, respectively (Figure 7I). Thus, in the absence of BCL11A expression, *Bcl11a*-mDA neurons became even more vulnerable to neurodegeneration, consistent with the protective role of BCL11A-mediated transcription described in the previous section. Interestingly, in *Bcl11a* cko^{lacZ} mice, neuronal cell death also affected β-gal^- mDA neurons. This latter finding suggests that inactivation of *Bcl11a* may have cell non-autonomous effects resulting in widespread deleterious consequences for nigral tissue integrity.

To further explore the vulnerability of *Bcl11a*-expressing SNc-mDA neurons to toxic insults, we analyzed scRNA-seq data from hiPSC-derived mDA neurons that were treated with rotenone to induce oxidative stress (Fernandes et al., 2020). Rotenone treatment significantly reduced the proportion of SNc-like mDA neurons (DAn1; Figure 2A). Further investigation highlighted a subpopulation of DAn1 cells sensitive to rotenone. Because

(C–D″) Immunostaining for β-gal and TH on coronal sections of P0 (C–C″) and P30 (D–D″) *Bcl11a* cko^{lacZ} mice.
(E and F) Quantification of TH^+ β-gal^+ neurons, expressed as the percentage of control (*Bcl11a-lacZ* mice; control values in Figures 1S and 1T). (E) At P0, the percentage of mDA neurons expressing β-gal in *Bcl11a* cko^{lacZ} mice (n = 5) is not significantly changed compared to that of *Bcl11a-lacZ* mice (n = 5). (F) At P30, the percentage of *Bcl11a*-mDA neurons is significantly increased in the CLi of *Bcl11a* cko^{lacZ} mice (n = 6) as compared to those of *Bcl11a-lacZ* mice (n = 6).
(G) Relative contribution of β-gal-positive TH neurons to the medial and lateral SNc at different rostrocaudal midbrain levels at P30. In *Bcl11a* cko^{lacZ} mice, there is a significant medial-to-lateral shift in the position of *Bcl11a*-mDA neurons at the most rostral level of the SNc. Statistical significance was determined by ANOVA followed by Šídák's multiple comparison test (F) and Welch's ANOVA followed by Dunnett's T3 multiple comparison test (G). *$p < 0.05$. Error bars indicate mean ± SEM. Scale bars: 200 μm (C–C″) and 500 μm (D–D‴). See also Figures S6 and S7.

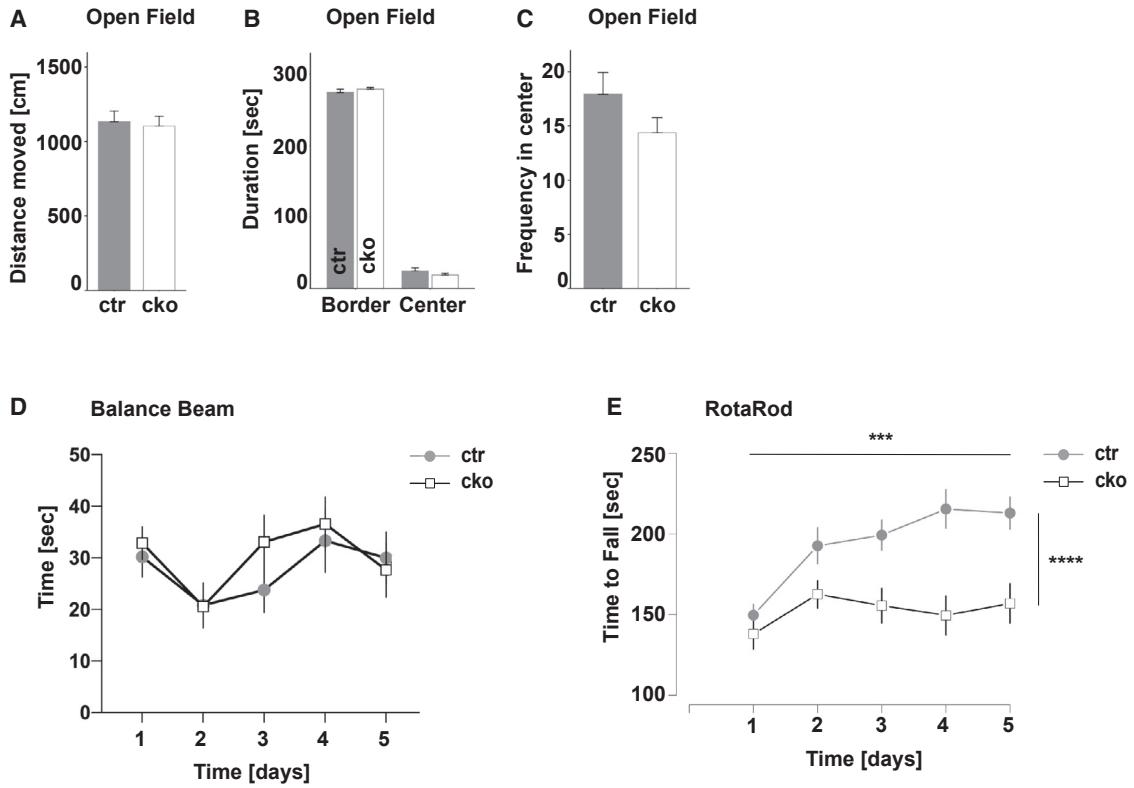

Figure 6. Inactivation of *Bcl11a* in mDA neurons results in specific defects in learned motor behavior

(A–C) Open field test (5-min time window) revealed no significant difference between *Bcl11a* cko^{flox} (cko) and control mice (ctr) in distance moved (A), in time spent in the center or border area (B), or the frequency of entering the center (C).

(D) Mice had to balance on a beam toward a food reward. The test was performed on 5 consecutive days. The ability of *Bcl11a* cko to cross a balance beam was not impaired.

(E) The rotarod test revealed that *Bcl11a* cko mice were not able to learn the motor task because the time to fall did not increase in *Bcl11a* cko mice within the 5 days of the trial period. *Bcl11a* cko (n = 12) and control mice (n = 13). Significance was determined by two-way ANOVA. ***p < 0.001, ****p < 0.0001. p = 7.226e-10 for genotype, p = 0.0002017 for days, and p = 0.0076354 for interdependence between days and genotypes. Error bars indicate mean ± SEM.

this subpopulation was absent from the rotenone-treated culture, we inferred those sensitive cells by mapping transcriptomes from the treated DAn1 cells to the untreated culture population. Cells with no pair in the untreated population were considered sensitive to rotenone. Interestingly, these rotenone-sensitive DAn1 cells had a distinct transcriptomic profile, with BCL11A more likely to be detected within single cells in this group than the rest of the non-sensitive DAn1 cells (*BCL11A*-negative cells: 407 depleted, 495 survived; *BCL11A*-positive cells: 83 depleted, 63 survived; Fisher's exact test for count data, p value = 0.00945). Together with our results from the *Bcl11a-lacZ* mice, these data indicate that both in mouse brain and in human *in vitro* models the *Bcl11a*/*BCL11A*-expressing mDA-SNc neuronal subpopulation is more susceptible to toxic insults than other mDA-SNc neuronal populations.

DISCUSSION

mDA neurons are diverse in their gene expression, their anatomical location, their projection targets, and their electrophysiological and functional properties (Farassat et al., 2019; Morales and Margolis, 2017; Poulin et al., 2020; Roeper, 2013). How these different features of mDA diversity are related is not yet clear but is the subject of intense research. For example, a number of recent studies have shown that subsets of mDA neurons sharing expression of specific markers have also specific projection targets in the forebrain (Bimpisidis et al., 2019; Heymann et al., 2020; Khan et al., 2017; Kramer et al., 2018; Poulin et al., 2018). However, how and whether such subsets are already defined during development remain unclear.

Here, we show that the expression of the transcription factor BCL11A defines subpopulations of mDA neurons starting from embryogenesis and throughout adulthood in the mouse and in iPSC-derived human mDA neurons. *Bcl11a* is expressed in many types of neurons in almost every region of the CNS (Allen Brain Atlas), but its function has been studied only in a few regions so far (Simon et al., 2020). In the cortex, BCL11A is important for the specification of cortical neurons that project to subcerebral areas (Cánovas et al., 2015; Woodworth et al., 2016), and it controls the acquisition of sensory area identity and the establishment of sensory input fields (Greig et al., 2016). Moreover, BCL11A regulates the migration of cortical projecting neurons (Wiegreffe et al., 2015). In the dorsal spinal cord, BCL11A is required for neuronal morphogenesis and sensory

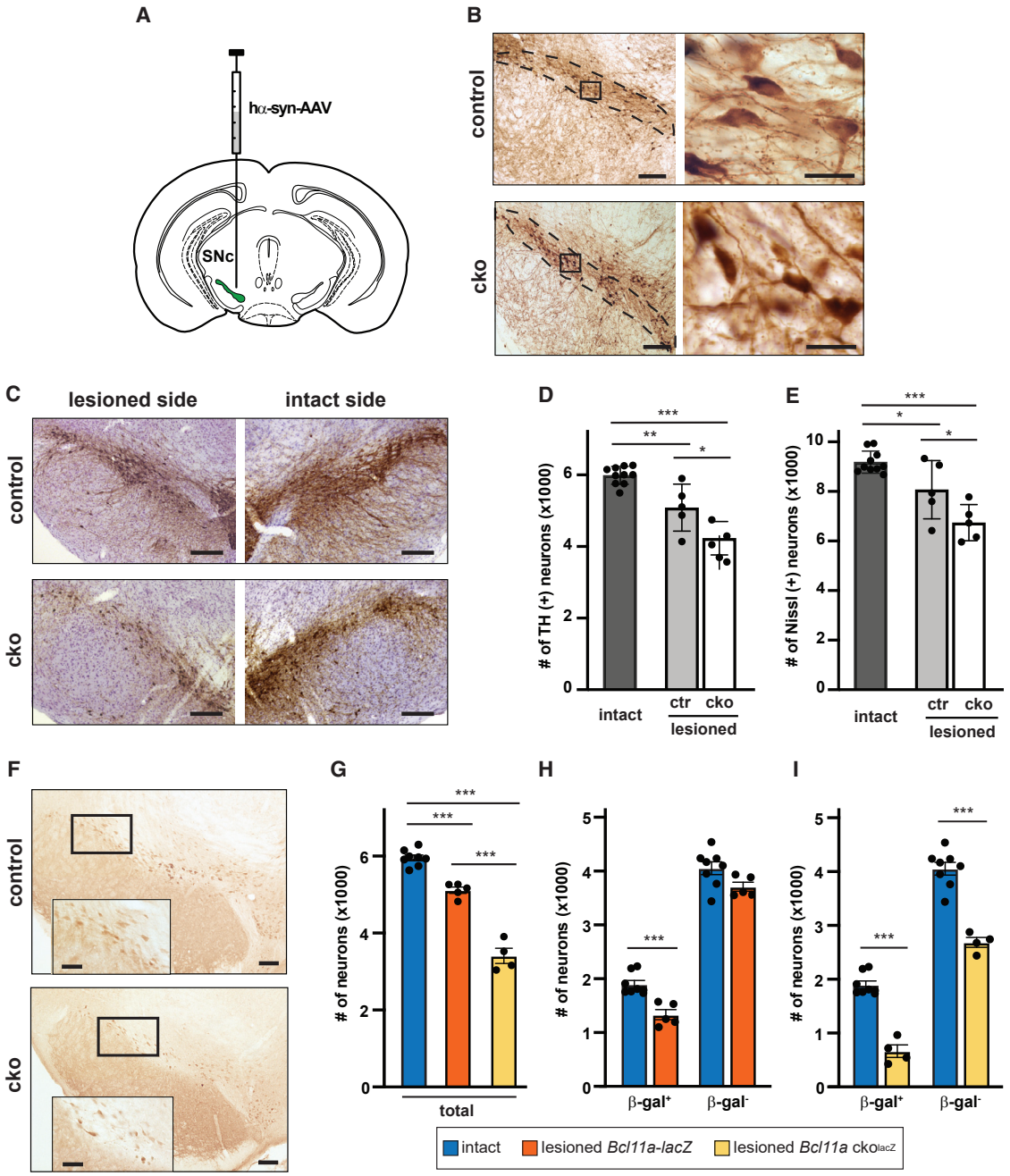

Figure 7. α-Synuclein toxicity is enhanced in the absence of BCL11A

(A) Mice received a unilateral intraparenchymal injection of rAAVs carrying the DNA for human α-synuclein (hα-syn) into the SNc.

(B–F) Control (n = 5) and *Bcl11a* cko (n = 5) mice were sacrificed 8 weeks after treatment with hα-syn-AAVs. (B) Midbrain coronal sections comprising the SNc (delineated with dotted lines at low magnification) were immunostained with anti-human α-synuclein antibody to detect expression of the transduced protein in control and *Bcl11a* cko mice. Right panels: higher magnification of the boxed areas. (C) Midbrain sections were immunostained for TH (brown staining) and counterstained with cresyl violet (purple). Left panels: lesioned (AAV-injected) sides. Right panels: contralateral intact sides. (D and E) TH-immunoreactive (D) and Nissl-stained (E) neurons were counted stereologically in the intact (left) and lesioned (right) SNc of control (n = 5) and *Bcl11a* cko (n = 5) mice. Intact side values from control and cko animals were pooled (dark gray bars). Light-gray and empty bars show average values from the lesioned side of control (ctr) and cko mice, respectively. (F) Midbrain sections were immunostained for p129 α-synuclein. Representative images show labeled mDA cell bodies in the SNc; the square boxes encompass areas of the SNc that are shown at higher magnification (insets).

(G–I) *Bcl11a-lacZ* control (n = 5) and *Bcl11a* cko^{lacZ} (n = 4) mice were sacrificed 8 weeks after treatment with hα-syn-AAVs. Midbrain sections from *Bcl11a-lacZ* control (n = 5) and *Bcl11a* cko^{lacZ} (n = 4) mice were double stained with anti-TH and anti-β-gal antibodies. (G) Total neurons (β-gal-negative and β-gal-positive TH cells) were counted in the SNc of *Bcl11a-lacZ* and *Bcl11a* cko^{lacZ} mice using confocal stereology. (H) The number of TH/β-gal-positive and TH/β-gal-negative

(legend continued on next page)

circuit formation (John et al., 2012). Whether it functions purely as a transcriptional repressor or also as part of the chromatin remodeling complex in these neurons remains to be investigated (see Introduction). In mDA neurons, the inactivation of *Bcl11a* results in a rostral-to-caudal shift in the position of *Bcl11a*-mDA neurons in the VTA and a medial-to-lateral shift in the rostral SNc, suggesting that BCL11A might play a role in regulating the expression of factors that control the migration of mDA neurons. In the cerebral cortex, BCL11A regulates cortical neuron migration by controlling the expression of Semaphorin 3c (Wiegreffe et al., 2015), a cell adhesion molecule that is not expressed in mDA neurons (Kolk et al., 2009). An analysis of the scRNA-seq data for *BCL11A*-positive and *BCL11A*-negative cells in the hiPSC-derived DAn1 and DAn4 population showed that in *BCL11A*-positive cells, genes encoding components of the cytoskeleton or cytoskeleton-associated proteins known to be involved in the regulation of neuronal migration are differentially expressed (e.g., doublecortin-like kinase, neuronal navigator 1, tubulin beta 2 chain in DAn1; Rac1, microtubule associated protein 1B and tubulin beta 2 chain in DAn4) (Breuss et al., 2017; Deuel et al., 2006; Kawauchi, 2015; Koizumi et al., 2006; Sánchez-Huertas et al., 2020; Villarroel-Campos and Gonzalez-Billault, 2014).Thus, inactivation of *Bcl11a* in mDA neurons could result in changes in cytoskeleton dynamics that contribute to altered neuronal migration and positioning of mDA neurons in *Bcl11a* cko mice.

In humans, pathogenic variants of *BCL11A* (mostly *de novo* mutations) result in neurodevelopmental disorders that have recently been classified as BCL11A-related intellectual disabilities (Peron et al., 2019). This syndrome is characterized by general developmental delay, microcephaly, speech delay, and behavioral problems, as well as several non-CNS-related phenotypes. In some affected individuals, seizures or autism spectrum disorder have been reported. Given the widespread expression of *BCL11A* in the brain, it is unclear if any of these neurological symptoms in patients are associated with functional deficits in the DA system. Moreover, there are no reports of neurodegenerative phenotypes, but long-term observations of patients or case studies in adult or aged patients are not available, due to the limited number of cases reported and the bias toward diagnosis in childhood (Peron et al., 2019).

DA subcircuits may encode a precise behavioral output by targeting a set of substructures within the DA projection targets, and a few studies have shown that specific subcircuits within the mDA system regulate very specific aspects of behavior (Engelhard et al., 2019; Heymann et al., 2020; Menegas et al., 2018). Whether such behavioral modules are consistent with genetically determined populations is just starting to be examined (Heymann et al., 2020). *Bcl11a*-mDA neurons of the VTA project to the medial and ventral shell of the NAc and the OT, whereas *Bcl11a*-mDA neurons of the SN show a highly selective innervation of the ventral TS and the caudal DMS. This specific innervation pattern suggests that this genetically defined subpopulation may modulate a specific subset of dopamine-influenced behaviors. Indeed, inactivation of *Bcl11a* in mDA neurons results in a specific behavioral impairment in skilled motor learning, whereas spontaneous motor behavior or coordination is not affected. Because *Bcl11a* is specifically inactivated in mDA neurons in our conditional knockout mouse model, this behavioral phenotype is most likely caused by functional changes in mDA neurons rather than by deficits in other midbrain neurons, cerebellum, or motor cortex (Hikosaka et al., 2002; Li et al., 2017). Potential functional changes upon *Bcl11a* inactivation in mDA neurons, such as altered neuronal activity and/or a decrease in dopamine release, are apparently severe enough to elicit a behavioral phenotype. It will have to be explored in the future how *Bcl11a* inactivation alters *Bcl11a*-mDA neurons at a functional level. Such studies are complicated by the fact that only relatively small areas are densely innervated by *Bcl11a*-mDA neurons and that *Bcl11a*-mDA neurons constitute only a subset of mDA neurons. To date, BCL11A has not been directly linked to the regulation of neuronal activity. However, the fact that haploinsufficiency for *BCL11A* in humans leads to intellectual disability and *BCL11A* is a risk gene for autism spectrum disorder (as described above) indicate that BCL11A may influence neuronal activity not only by affecting brain development but also by directly regulating the expression of genes important for neuronal function in mature neurons (Peron et al., 2019; Satterstrom et al., 2020). Another line of evidence supporting a function of *Bcl11* genes in regulating neuronal activity comes from studies of the closely related *Bcl11b* in hippocampal neurons. Inactivation of *Bcl11b* in the adult brain leads to changes in hippocampal synapse formation and maintenance as well as electrophysiological deficits (e.g., massively impaired LTP) (De Bruyckere et al., 2018; Simon et al., 2016).

Dopamine release in the dorsal striatum appears to be essential for learning skilled motor behavior. Partial ablation of mDA projections using 6-hydroxydopamine (6-OHDA) in rats does not affect spontaneous motor behavior in the open field or on balance beam, but it strongly interferes with the ability of the animals to improve their performance on the rotarod (Ogura et al., 2005). Recent evidence suggests that the precise timing of dopamine signals influences the performance of highly skilled motor behavior in an immediate and a long-term manner (Bova et al., 2020). It has been proposed that the plasticity in striatal medium spiny neurons underlying initial skill learning during goal-directed actions requires dopamine release in the DMS, whereas dopamine release in the DLS is important for optimal skill learning (Durieux et al., 2012; Graybiel, 2008). Based on this model and our observation that *Bcl11a*-mDA neurons in the SNc project to the DMS but not the DLS, the deficit in motor learning could have its origin in the inability of the mice to initiate the learning of skilled motor behavior. Interestingly, the ablation of *Aldh1a1*-expressing mDA neurons leads to an impairment in motor skill learning on the rotarod that is similar to the one observed in *Bcl11a* cko mice even though *Aldh1a1*-expressing neurons project almost exclusively to the DLS (Wu et al., 2019). Thus, it is

neurons was counted in the SNc of *Bcl11a-lacZ* mice. (I) The number of TH/β-gal-positive and TH/β-gal-negative neurons was counted in the SNc of *Bcl11a* cko^{lacZ} animals. For these analyses, counts in the intact SNc showed no difference between the two groups of animals and were therefore pooled. Significance was determined by one-way ANOVA followed by Tukey's post hoc test for multiple comparisons (D, E, and G) or Student's t test (H and I). Error bars indicate mean ± SEM. Scale bars: 100 μm (low-magnification panels in B, C, and F), 20 μm (higher magnification panels in B), and 50 μm (higher magnification panels in F).

possible that altered dopamine release either in DMS and DLS and thus defects in both phases of learning lead to a similar overall defect in the acquisition of skill learning.

The mDA neurons in the ventral tier of the SNc have been characterized as being most vulnerable to neurodegeneration in PD as well as in animal models of the disease (Surmeier et al., 2017). Based on some PD models in rodents, the most vulnerable population appears to coincide with ALDH1A1-expressing SNc-mDA neurons (Poulin et al., 2014). On the other hand, ALDH1A1-negative SNc-mDA neurons are more vulnerable to overexpression of α-synuclein with a disease-relevant mutation (α-synuclein A53T) in a transgenic mouse model (Liu et al., 2014). Here, we demonstrate that *Bcl11a*-mDA neurons in the SNc, which are mostly located in the dorsal tier and are largely ALDH1A1 negative, are highly susceptible to neurodegeneration upon α-synuclein overexpression (mouse) or rotenone exposure (human). Thus, our data suggest that there are also differences in the vulnerability of mDA neurons within the dorsal tier of the SNc and that BCL11A serves as a marker for the more vulnerable mDA neuronal population within the dorsal tier. In the mouse brain, these *Bcl11a*-mDA neurons project to the caudal DMS, which corresponds roughly to the caudate nucleus in the human brain (Burton et al., 2015). Some of the early symptoms associated with PD are assumed to be based on functional deficits of the caudate nucleus (rapid eye movement sleep behavior disorder and gait problems), and a recent study demonstrated a significant DA de-innervation of the caudate nucleus in about one-half of the examined patients in the early stage of PD (Pasquini et al., 2019), suggesting that caudate-projecting mDA neurons may also form a vulnerable population in humans. *BCL11A* is expressed in hiPSC-derived mDA neurons (our data) and in human mDA neurons (La Manno et al., 2016), but further studies will be necessary to evaluate which subpopulations express this transcription factor in the human DA system and whether the reduced DA innervation of the caudate nucleus in early PD may be associated with a specific loss of *BCL11A*-expressing mDA neurons in patients.

Although *Bcl11a*-mDA SNc neurons are more susceptible to α-synuclein-induced degeneration, BCL11A also acts as a neuroprotective factor in this population because the loss of *Bcl11a*-mDA neurons is significantly more severe in *Bcl11a* cko^{lacZ} mice than in *Bcl11a-lacZ* mice. BCL11A could be modulating cell survival directly because it has been shown to regulate expression of the anti-apoptotic factor BCL2 in early B lymphocytes and inactivation of *Bcl11a* in cortical projection neurons results in increased cell death (Wiegreffe et al., 2015; Yu et al., 2012). An analysis of scRNA-seq data of *BCL11A*-positive and *BCL11A*-negative cells in the DAn1 population shows that several genes or pathways that have previously been implicated in neurodegenerative processes are differentially expressed in *BCL11A*-positive neurons. These include genes encoding for microtubule-associated proteins (described above: doublecortin-like kinase, neuronal navigator 1, and tubulin beta 2 chain). By regulating the expression of these genes, BCL11A could affect the balance between stable and dynamic microtubules. Because perturbances in microtubule dynamics might contribute to neurodegenerative processes, this could be one potential pathway regulated by BCL11A contributing to its role as a neuroprotective factor (Calogero et al., 2019; Dubey et al., 2015). In addition, we find that *NSC1* (*neuronal Ca^{2+} sensor 1*) transcripts are upregulated in the *BCL11A*-expressing human DAn1 population. NCS1 acts as a neuroprotective factor potentially by shielding SNc-mDA neurons from Ca^{2+} overload, which arises from the particular activity patterns (pacemaker activity) and low Ca^{2+} buffering capacities of SNc-mDA neurons. Inactivation of NCS1 in mice aggravates neurodegeneration in the SNc, and NCS1 levels are reduced in iPSC-derived mDA neurons from patients with familiar PD (Benkert et al., 2019; Surmeier et al., 2017). If BCL11A positively regulates NCS1 expression, a loss of BCL11A could lead to reduced NSC1 levels, which could contribute to increased susceptibility of these neurons to neurodegeneration. Future studies will have to investigate whether these mechanisms underlie the function of BCL11A in neurodegeneration and neuroprotection in both mouse and human mDA neurons.

CONCLUSIONS

Our data demonstrate that the expression of *Bcl11a* defines subpopulations of mDA neurons in the SNc and VTA that form a highly specific subcircuit within the DA system. We show in the mouse DA system and in hiPSC-derived mDA neurons that the *Bcl11a*-expressing mDA neurons in the SNc show distinct susceptibility to toxic insults. The loss of BCL11A function in these neurons interferes with their functional integrity and their resilience to neurodegeneration. It will be of great interest to investigate whether the subcircuits formed by *Bcl11a*-expressing mDA neurons comprise a specific functional module in the DA system and to understand the gene regulatory networks downstream of BCL11a that affect the (patho)physiology of this subpopulation of mDA neurons.

STAR★METHODS

Detailed methods are provided in the online version of this paper and include the following:

- KEY RESOURCES TABLE
- RESOURCE AVAILABILITY
  - Lead contact
  - Materials availability
  - Data and code availability
- EXPERIMENTAL MODEL AND SUBJECT DETAILS
  - Tamoxifen administration
  - Tissue processing
  - Multiplex fluorescent *in situ* hybridization
  - Stereotactic viral vector injection
  - Image acquisition
  - Quantification of cell numbers
  - Stereology
  - Analysis of fiber density
  - Behavioral tests
  - Single cell RNA-sequencing
- STATISTICAL ANALYSIS

SUPPLEMENTAL INFORMATION

Supplemental information can be found online at https://doi.org/10.1016/j.celrep.2021.109697.

ACKNOWLEDGMENTS

This work was supported by the German Research Foundation (BL 767/2–1, BL 767/3–1, BL 767/4–1, 417960915 to S. Blaess), the SFB 1089 (to M.T., S. Blaess, and K.M.J.v.L.), the Maria von Linden-Program (University of Bonn to S. Blaess), and the Ministerium für Kultur und Wissenschaft des Landes Nordrhein-Westfalen (Rückkehrer-Programm to S. Blaess). Further support was obtained from the Innovative Medicines Initiative 2 (IMI-2 821522; PD-MitoQUANT to D.A.D.M.), and EU Joint Programme-Neurodegenerative Disease (JPND 01ED2005B to D.A.D.M.). N.P. has been supported by UK Dementia Research Institute grant RRZA/175. S. Britsch has been supported by grants from the German Research Foundation (BR 2215/1-1 and 2215/1-2). We thank Neal Copeland and Nancy Jenkins for agreeing to provide the *Bcl11a* floxed mouse line; the UKB microscopy core facility for support with imaging; the UKB virus core for providing AAVs; Milan Pabst and Heinz Beck for support with stereotactical injections; Alesja Dernst, Philipp Grunwald, and Julian Wirtz for technical support; and Norisa Meli for critical reading of the manuscript. The graphical abstract was created with biorender.com.

AUTHOR CONTRIBUTIONS

M.T., data curation, formal analysis, validation, investigation, visualization, methodology, writing—original draft, writing—review and editing; A.U., data curation, formal analysis, validation, investigation, visualization, methodology, writing—review and editing; K.U.S.I., investigation, visualization, methodology, writing—review and editing; N.P., data analysis—single-cell transcriptomics, visualization—single-cell transcriptomics, methodology—single-cell transcriptomics, writing—review and editing; G.O.B., investigation, visualization, methodology, writing—review and editing; E.Ö., B.B., A.M., and A.W., investigation, writing—review and editing; S. Britsch, P.L., W.T.K., and K.M.J.v. Loo, resources, writing—review and editing; E.M., data curation, resources, writing—review and editing; S. Baader, data curation, formal analysis, validation, resources, methodology, writing—review and editing; D.A.D.M., data curation, formal analysis, validation, resources, writing—review and editing; S. Blaess, conceptualization, resources, data curation, formal analysis, supervision, funding acquisition, validation, methodology, project administration, writing—original draft, writing—review and editing.

DECLARATION OF INTERESTS

The authors declare no competing interests.

Received: March 13, 2021
Revised: July 8, 2021
Accepted: August 18, 2021
Published: September 14, 2021

REFERENCES

Alvarez-Bolado, G., Paul, F.A., and Blaess, S. (2012). Sonic hedgehog lineage in the mouse hypothalamus: from progenitor domains to hypothalamic regions. Neural Dev. *7*, 4.

Bäckman, C.M., Malik, N., Zhang, Y., Shan, L., Grinberg, A., Hoffer, B.J., Westphal, H., and Tomac, A.C. (2006). Characterization of a mouse strain expressing Cre recombinase from the 3′ untranslated region of the dopamine transporter locus. Genesis *44*, 383–390.

Basak, A., Hancarova, M., Ulirsch, J.C., Balci, T.B., Trkova, M., Pelisek, M., Vlckova, M., Muzikova, K., Cermak, J., Trka, J., et al. (2015). BCL11A deletions result in fetal hemoglobin persistence and neurodevelopmental alterations. J. Clin. Invest. *125*, 2363–2368.

Benkert, J., Hess, S., Roy, S., Beccano-Kelly, D., Wiederspohn, N., Duda, J., Simons, C., Patil, K., Gaifullina, A., Mannal, N., et al. (2019). Cav2.3 channels contribute to dopaminergic neuron loss in a model of Parkinson's disease. Nat. Commun. *10*, 5094.

Bimpisidis, Z., König, N., Stagkourakis, S., Zell, V., Vlcek, B., Dumas, S., Giros, B., Broberger, C., Hnasko, T.S., and Wallén-Mackenzie, Å. (2019). The NeuroD6 subtype of VTA neurons contributes to psychostimulant sensitization and behavioral reinforcement. Eneuro *6*, ENEURO.0066-19.2019.

Bova, A., Gaidica, M., Hurst, A., Iwai, Y., Hunter, J., and Leventhal, D.K. (2020). Precisely timed dopamine signals establish distinct kinematic representations of skilled movements. eLife *9*, e61591.

Breuss, M.W., Leca, I., Gstrein, T., Hansen, A.H., and Keays, D.A. (2017). Tubulins and brain development - The origins of functional specification. Mol. Cell. Neurosci. *84*, 58–67.

Burton, A.C., Nakamura, K., and Roesch, M.R. (2015). From ventral-medial to dorsal-lateral striatum: neural correlates of reward-guided decision-making. Neurobiol. Learn. Mem. *117*, 51–59.

Calogero, A.M., Mazzetti, S., Pezzoli, G., and Cappelletti, G. (2019). Neuronal microtubules and proteins linked to Parkinson's disease: a relevant interaction? Biol. Chem. *400*, 1099–1112.

Cánovas, J., Berndt, F.A., Sepúlveda, H., Aguilar, R., Veloso, F.A., Montecino, M., Oliva, C., Maass, J.C., Sierralta, J., and Kukuljan, M. (2015). The Specification of Cortical Subcerebral Projection Neurons Depends on the Direct Repression of TBR1 by CTIP1/BCL11a. J. Neurosci. *35*, 7552–7564.

Carter, R.J., Lione, L.A., Humby, T., Mangiarini, L., Mahal, A., Bates, G.P., Dunnett, S.B., and Morton, A.J. (1999). Characterization of progressive motor deficits in mice transgenic for the human Huntington's disease mutation. J. Neurosci. *19*, 3248–3257.

Chen, L., Xie, Z., Turkson, S., and Zhuang, X. (2015). A53T human α-synuclein overexpression in transgenic mice induces pervasive mitochondria macroautophagy defects preceding dopamine neuron degeneration. J. Neurosci. *35*, 890–905.

Costa, R.M., Cohen, D., and Nicolelis, M.A.L. (2004). Differential corticostriatal plasticity during fast and slow motor skill learning in mice. Curr. Biol. *14*, 1124–1134.

Cox, J., and Witten, I.B. (2019). Striatal circuits for reward learning and decision-making. Nat. Rev. Neurosci. *20*, 482–494.

De Bruyckere, E., Simon, R., Nestel, S., Heimrich, B., Kätzel, D., Egorov, A.V., Liu, P., Jenkins, N.A., Copeland, N.G., Schwegler, H., et al. (2018). Stability and Function of Hippocampal Mossy Fiber Synapses Depend on *Bcl11b/Ctip2*. Front. Mol. Neurosci. *11*, 103.

Deuel, T.A.S., Liu, J.S., Corbo, J.C., Yoo, S.-Y., Rorke-Adams, L.B., and Walsh, C.A. (2006). Genetic interactions between doublecortin and doublecortin-like kinase in neuronal migration and axon outgrowth. Neuron *49*, 41–53.

Dias, C., Estruch, S.B., Graham, S.A., McRae, J., Sawiak, S.J., Hurst, J.A., Joss, S.K., Holder, S.E., Morton, J.E.V., Turner, C., et al.; DDD Study (2016). BCL11A Haploinsufficiency Causes an Intellectual Disability Syndrome and Dysregulates Transcription. Am. J. Hum. Genet. *99*, 253–274.

Dodson, P.D., Dreyer, J.K., Jennings, K.A., Syed, E.C.J., Wade-Martins, R., Cragg, S.J., Bolam, J.P., and Magill, P.J. (2016). Representation of spontaneous movement by dopaminergic neurons is cell-type selective and disrupted in parkinsonism. Proc. Natl. Acad. Sci. USA *113*, E2180–E2188.

Dubey, J., Ratnakaran, N., and Koushika, S.P. (2015). Neurodegeneration and microtubule dynamics: death by a thousand cuts. Front. Cell. Neurosci. *9*, 343.

Durieux, P.F., Schiffmann, S.N., and de Kerchove d'Exaerde, A. (2012). Differential regulation of motor control and response to dopaminergic drugs by D1R and D2R neurons in distinct dorsal striatum subregions. EMBO J. *31*, 640–653.

El Yacoubi, M., Bouali, S., Popa, D., Naudon, L., Leroux-Nicollet, I., Hamon, M., Costentin, J., Adrien, J., and Vaugeois, J.-M. (2003). Behavioral, neurochemical, and electrophysiological characterization of a genetic mouse model of depression. Proc. Natl. Acad. Sci. USA *100*, 6227–6232.

Engelhard, B., Finkelstein, J., Cox, J., Fleming, W., Jang, H.J., Ornelas, S., Koay, S.A., Thiberge, S.Y., Daw, N.D., Tank, D.W., and Witten, I.B. (2019). Specialized coding of sensory, motor and cognitive variables in VTA dopamine neurons. Nature *570*, 509–513.

Farassat, N., Costa, K.M., Stojanovic, S., Albert, S., Kovacheva, L., Shin, J., Egger, R., Somayaji, M., Duvarci, S., Schneider, G., and Roeper, J. (2019). In vivo functional diversity of midbrain dopamine neurons within identified axonal projections. eLife *8*, e48408.

Fernandes, H.J.R., Patikas, N., Foskolou, S., Field, S.F., Park, J.E., Byrne, M.L., Bassett, A.R., and Metzakopian, E. (2020). Single-Cell Transcriptomics of Parkinson's Disease Human In Vitro Models Reveals Dopamine Neuron-Specific Stress Responses. Cell Rep. *33*, 108263.

Fitzgerald, T.W., Gerety, S.S., Jones, W.D., van Kogelenberg, M., King, D.A., McRae, J., Morley, K.I., Parthiban, V., Al-Turki, S., Ambridge, K., et al.; Deciphering Developmental Disorders Study (2015). Large-scale discovery of novel genetic causes of developmental disorders. Nature *519*, 223–228.

Franklin, K.B.J., and Paxinos, G. (2007). The Mouse Brain in Stereotaxic Coordinates, Third Edition (Academic Press).

Fujiwara, H., Hasegawa, M., Dohmae, N., Kawashima, A., Masliah, E., Goldberg, M.S., Shen, J., Takio, K., and Iwatsubo, T. (2002). α-Synuclein is phosphorylated in synucleinopathy lesions. Nat. Cell Biol. *4*, 160–164.

Goedert, M., Spillantini, M.G., Del Tredici, K., and Braak, H. (2013). 100 years of Lewy pathology. Nat. Rev. Neurol. *9*, 13–24.

Graybiel, A.M. (2008). Habits, rituals, and the evaluative brain. Annu. Rev. Neurosci. *31*, 359–387.

Greig, L.C., Woodworth, M.B., Greppi, C., and Macklis, J.D. (2016). Ctip1 Controls Acquisition of Sensory Area Identity and Establishment of Sensory Input Fields in the Developing Neocortex. Neuron *90*, 261–277.

Gundersen, H.J.G., and Jensen, E.B. (1987). The efficiency of systematic sampling in stereology and its prediction. J. Microsc. *147*, 229–263.

Helwig, M., Klinkenberg, M., Rusconi, R., Musgrove, R.E., Majbour, N.K., El-Agnaf, O.M.A., Ulusoy, A., and Monte, D.A.D. (2016). Brain propagation of transduced α-synuclein involves non-fibrillar protein species and is enhanced in α-synuclein null mice. Brain *139*, 856–870.

Heymann, G., Jo, Y.S., Reichard, K.L., McFarland, N., Chavkin, C., Palmiter, R.D., Soden, M.E., and Zweifel, L.S. (2020). Synergy of Distinct Dopamine Projection Populations in Behavioral Reinforcement. Neuron *105*, 909–920.e5.

Hikosaka, O., Nakamura, K., Sakai, K., and Nakahara, H. (2002). Central mechanisms of motor skill learning. Curr. Opin. Neurobiol. *12*, 217–222.

John, A., Brylka, H., Wiegreffe, C., Simon, R., Liu, P., Jüttner, R., Crenshaw, E.B., 3rd, Luyten, F.P., Jenkins, N.A., Copeland, N.G., et al. (2012). Bcl11a is required for neuronal morphogenesis and sensory circuit formation in dorsal spinal cord development. Development *139*, 1831–1841.

Kadoch, C., Hargreaves, D.C., Hodges, C., Elias, L., Ho, L., Ranish, J., and Crabtree, G.R. (2013). Proteomic and bioinformatic analysis of mammalian SWI/SNF complexes identifies extensive roles in human malignancy. Nat. Genet. *45*, 592–601.

Kawauchi, T. (2015). Cellullar insights into cerebral cortical development: focusing on the locomotion mode of neuronal migration. Front. Cell. Neurosci. *9*, 394.

Khan, S., Stott, S.R.W., Chabrat, A., Truckenbrodt, A.M., Spencer-Dene, B., Nave, K.-A., Guillemot, F., Levesque, M., and Ang, S.-L. (2017). Survival of a Novel Subset of Midbrain Dopaminergic Neurons Projecting to the Lateral Septum Is Dependent on NeuroD Proteins. J. Neurosci. *37*, 2305–2316.

Koizumi, H., Tanaka, T., and Gleeson, J.G. (2006). Doublecortin-like kinase functions with doublecortin to mediate fiber tract decussation and neuronal migration. Neuron *49*, 55–66.

Kolk, S.M., Gunput, R.-A.F., Tran, T.S., van den Heuvel, D.M.A., Prasad, A.A., Hellemons, A.J., Adolfs, Y., Ginty, D.D., Kolodkin, A.L., Burbach, J.P.H., et al. (2009). Semaphorin 3F Is a Bifunctional Guidance Cue for Dopaminergic Axons and Controls Their Fasciculation, Channeling, Rostral Growth, and Intracortical Targeting. J. Neurosci. *29*, 12542–12557.

Kramer, D.J., Risso, D., Kosillo, P., Ngai, J., and Bateup, H.S. (2018). Combinatorial Expression of Grp and Neurod6 Defines Dopamine Neuron Populations with Distinct Projection Patterns and Disease Vulnerability. Eneuro *5*, ENEURO.0152-18.2018.

La Manno, G., Gyllborg, D., Codeluppi, S., Nishimura, K., Salto, C., Zeisel, A., Borm, L.E., Stott, S.R.W., Toledo, E.M., Villaescusa, J.C., et al. (2016). Molecular Diversity of Midbrain Development in Mouse, Human, and Stem Cells. Cell *167*, 566–580.e19.

Lerner, T.N., Shilyansky, C., Davidson, T.J., Evans, K.E., Beier, K.T., Zalocusky, K.A., Crow, A.K., Malenka, R.C., Luo, L., Tomer, R., and Deisseroth, K. (2015). Intact-Brain Analyses Reveal Distinct Information Carried by SNc Dopamine Subcircuits. Cell *162*, 635–647.

Li, Q., Ko, H., Qian, Z.-M., Yan, L.Y.C., Chan, D.C.W., Arbuthnott, G., Ke, Y., and Yung, W.-H. (2017). Refinement of learned skilled movement representation in motor cortex deep output layer. Nat. Commun. *8*, 15834.

Liu, G., Yu, J., Ding, J., Xie, C., Sun, L., Rudenko, I., Zheng, W., Sastry, N., Luo, J., Rudow, G., et al. (2014). Aldehyde dehydrogenase 1 defines and protects a nigrostriatal dopaminergic neuron subpopulation. J. Clin. Invest. *124*, 3032–3046.

Luong, T.N., Carlisle, H.J., Southwell, A., and Patterson, P.H. (2011). Assessment of motor balance and coordination in mice using the balance beam. J. Vis. Exp., 2376.

Madisen, L., Garner, A.R., Shimaoka, D., Chuong, A.S., Klapoetke, N.C., Li, L., van der Bourg, A., Niino, Y., Egolf, L., Monetti, C., et al. (2015). Transgenic mice for intersectional targeting of neural sensors and effectors with high specificity and performance. Neuron *85*, 942–958.

Menegas, W., Bergan, J.F., Ogawa, S.K., Isogai, Y., Umadevi Venkataraju, K., Osten, P., Uchida, N., and Watabe-Uchida, M. (2015). Dopamine neurons projecting to the posterior striatum form an anatomically distinct subclass. eLife *4*, e10032.

Menegas, W., Akiti, K., Amo, R., Uchida, N., and Watabe-Uchida, M. (2018). Dopamine neurons projecting to the posterior striatum reinforce avoidance of threatening stimuli. Nat. Neurosci. *21*, 1421–1430.

Migdalska-Richards, A., Wegrzynowicz, M., Rusconi, R., Deangeli, G., Di Monte, D.A., Spillantini, M.G., and Schapira, A.H.V. (2017). The L444P Gba1 mutation enhances alpha-synuclein induced loss of nigral dopaminergic neurons in mice. Brain *140*, 2706–2721.

Morales, M., and Margolis, E.B. (2017). Ventral tegmental area: cellular heterogeneity, connectivity and behaviour. Nat. Rev. Neurosci. *18*, 73–85.

Musgrove, R.E., Helwig, M., Bae, E.-J., Aboutalebi, H., Lee, S.-J., Ulusoy, A., and Di Monte, D.A. (2019). Oxidative stress in vagal neurons promotes parkinsonian pathology and intercellular α-synuclein transfer. J. Clin. Invest. *129*, 3738–3753.

Ogura, T., Ogata, M., Akita, H., Jitsuki, S., Akiba, L., Noda, K., Hoka, S., and Saji, M. (2005). Impaired acquisition of skilled behavior in rotarod task by moderate depletion of striatal dopamine in a pre-symptomatic stage model of Parkinson's disease. Neurosci. Res. *51*, 299–308.

Panman, L., Papathanou, M., Laguna, A., Oosterveen, T., Volakakis, N., Acampora, D., Kurtsdotter, I., Yoshitake, T., Kehr, J., Joodmardi, E., et al. (2014). Sox6 and Otx2 control the specification of substantia nigra and ventral tegmental area dopamine neurons. Cell Rep. *8*, 1018–1025.

Pasquini, J., Durcan, R., Wiblin, L., Gersel Stokholm, M., Rochester, L., Brooks, D.J., Burn, D., and Pavese, N. (2019). Clinical implications of early caudate dysfunction in Parkinson's disease. J. Neurol. Neurosurg. Psychiatry *90*, 1098–1104.

Pensa, S., Liu, P., and Khaled, W.T. (2021). The generation of a Bcl11a lineage tracing mouse model. bioRxiv. https://doi.org/10.1101/2021.07.26.453822.

Peron, A., Bradbury, K., Viskochil, D.H., and Dias, C. (2019). BCL11A -Related Intellectual Disability (Gene Reviews).

Poulin, J.-F., Zou, J., Drouin-Ouellet, J., Kim, K.-Y.A., Cicchetti, F., and Awatramani, R.B. (2014). Defining midbrain dopaminergic neuron diversity by single-cell gene expression profiling. Cell Rep. *9*, 930–943.

Poulin, J.-F., Caronia, G., Hofer, C., Cui, Q., Helm, B., Ramakrishnan, C., Chan, C.S., Dombeck, D.A., Deisseroth, K., and Awatramani, R. (2018). Mapping projections of molecularly defined dopamine neuron subtypes using intersectional genetic approaches. Nat. Neurosci. *21*, 1260–1271.

Poulin, J.-F., Gaertner, Z., Moreno-Ramos, O.A., and Awatramani, R. (2020). Classification of Midbrain Dopamine Neurons Using Single-Cell Gene Expression Profiling Approaches. Trends Neurosci. *43*, 155–169.

Roeper, J. (2013). Dissecting the diversity of midbrain dopamine neurons. Trends Neurosci. *36*, 336–342.

Sánchez-Huertas, C., Bonhomme, M., Falco, A., Fagotto-Kaufmann, C., van Haren, J., Jeanneteau, F., Galjart, N., Debant, A., and Boudeau, J. (2020). The +TIP Navigator-1 is an actin-microtubule crosslinker that regulates axonal growth cone motility. J. Cell Biol. *219*, e201905199.

Satterstrom, F.K., Kosmicki, J.A., Wang, J., Breen, M.S., De Rubeis, S., An, J.-Y., Peng, M., Collins, R., Grove, J., Klei, L., et al.; Autism Sequencing Consortium; iPSYCH-Broad Consortium (2020). Large-Scale Exome Sequencing Study Implicates Both Developmental and Functional Changes in the Neurobiology of Autism. Cell *180*, 568–584.e23.

Simon, R., Baumann, L., Fischer, J., Seigfried, F.A., De Bruyckere, E., Liu, P., Jenkins, N.A., Copeland, N.G., Schwegler, H., and Britsch, S. (2016). Structure-function integrity of the adult hippocampus depends on the transcription factor Bcl11b/Ctip2. Genes Brain Behav. *15*, 405–419.

Simon, R., Wiegreffe, C., and Britsch, S. (2020). Bcl11 Transcription Factors Regulate Cortical Development and Function. Front. Mol. Neurosci. *13*, 51.

Soblet, J., Dimov, I., Graf von Kalckreuth, C., Cano-Chervel, J., Baijot, S., Pelc, K., Sottiaux, M., Vilain, C., Smits, G., and Deconinck, N. (2018). BCL11A frameshift mutation associated with dyspraxia and hypotonia affecting the fine, gross, oral, and speech motor systems. Am. J. Med. Genet. A. *176*, 201–208.

Surmeier, D.J., Obeso, J.A., and Halliday, G.M. (2017). Selective neuronal vulnerability in Parkinson disease. Nat. Rev. Neurosci. *18*, 101–113.

Thompson, L., Barraud, P., Andersson, E., Kirik, D., and Björklund, A. (2005). Identification of dopaminergic neurons of nigral and ventral tegmental area subtypes in grafts of fetal ventral mesencephalon based on cell morphology, protein expression, and efferent projections. J. Neurosci. *25*, 6467–6477.

Tye, K.M., Mirzabekov, J.J., Warden, M.R., Ferenczi, E.A., Tsai, H.-C., Finkelstein, J., Kim, S.-Y., Adhikari, A., Thompson, K.R., Andalman, A.S., et al. (2013). Dopamine neurons modulate neural encoding and expression of depression-related behaviour. Nature *493*, 537–541.

Ulusoy, A., and Di Monte, D.A. (2013). α-Synuclein elevation in human neurodegenerative diseases: experimental, pathogenetic, and therapeutic implications. Mol. Neurobiol. *47*, 484–494.

Villarroel-Campos, D., and Gonzalez-Billault, C. (2014). The MAP1B case: an old MAP that is new again. Dev. Neurobiol. *74*, 953–971.

Wiegreffe, C., Simon, R., Peschkes, K., Kling, C., Strehle, M., Cheng, J., Srivatsa, S., Liu, P., Jenkins, N.A., Copeland, N.G., et al. (2015). Bcl11a (Ctip1) Controls Migration of Cortical Projection Neurons through Regulation of Sema3c. Neuron *87*, 311–325.

Wolf, F.A., Angerer, P., and Theis, F.J. (2018). SCANPY: large-scale single-cell gene expression data analysis. Genome Biol. *19*, 15.

Woodworth, M.B., Greig, L.C., Liu, K.X., Ippolito, G.C., Tucker, H.O., and Macklis, J.D. (2016). Ctip1 Regulates the Balance between Specification of Distinct Projection Neuron Subtypes in Deep Cortical Layers. Cell Rep. *15*, 999–1012.

Wu, J., Kung, J., Dong, J., Chang, L., Xie, C., Habib, A., Hawes, S., Yang, N., Chen, V., Liu, Z., et al. (2019). Distinct Connectivity and Functionality of Aldehyde Dehydrogenase 1a1-Positive Nigrostriatal Dopaminergic Neurons in Motor Learning. Cell Rep. *28*, 1167–1181.e7.

Yu, Y., Wang, J., Khaled, W., Burke, S., Li, P., Chen, X., Yang, W., Jenkins, N.A., Copeland, N.G., Zhang, S., and Liu, P. (2012). Bcl11a is essential for lymphoid development and negatively regulates p53. J. Exp. Med. *209*, 2467–2483.

Zhou, Y., Zhou, B., Pache, L., Chang, M., Khodabakhshi, A.H., Tanaseichuk, O., Benner, C., and Chanda, S.K. (2019). Metascape provides a biologist-oriented resource for the analysis of systems-level datasets. Nat. Commun. *10*, 1523.

STAR★METHODS

KEY RESOURCES TABLE

REAGENT or RESOURCE	SOURCE	IDENTIFIER
Antibodies		
goat anti-β-gal	Biogenesis, Kinsgton,NH, USA	Validated in Alvarez-Bolado et al., 2012
guinea pig anti-BCL11A	First described in John et al., 2012	N/A
mouse anti-human α-synuclein	Merck, Darmstadt, DE	RRID: AB_310817
mouse anti-TH	Merck, Darmstadt, DE	RRID:AB_2201528
rabbit anti-ALDH1A1	Sigma-Aldrich, St. Louis, MO, USA	RRID:AB_1844722
rabbit anti-Calbindin	Swant, Herford, DE	RRID:AB_2314067
rabbit anti-RFP	Rockland-inc, Hamburg, DE	RRID:AB_2209751
rabbit anti-SOX6	Abcam, Cambridge, UK	RRID:AB_1143033
rabbit anti-TH	Merck, Darmstadt, DE	RRID:AB_390204
rat anti-GFP	Nalacai Tesque, Kyoto, JP	RRID:AB_10013361
Cy3-Streptavidin	Jackson ImmunoResearch, Ely, Cambridgeshire, UK	RRID:**A**B_2337244
donkey anti-goat Cy3	Jackson ImmunoResearch, Ely, Cambridgeshire, UK	RRID:AB_2307351
donkey anti-guinea pig Biotin	Jackson ImmunoResearch, Ely, Cambridgeshire, UK	RRID:**A**B_2340451
donkey anti mouse-Alexa 488	Thermo Fischer Scientific, Waltham, MA, USA	RRID:**A**B_141607
donkey anti mouse-Alexa 647	Thermo Fischer Scientific, Waltham, MA, USA	RRID:**A**B_162542
donkey anti rabbit-Alexa 488	Thermo Fischer Scientific, Waltham, MA, USA	RRID:AB_2535792
donkey anti rabbit-Alexa 546	Thermo Fischer Scientific, Waltham, MA, USA	RRID:AB_2534016
donkey anti rabbit-Alexa 647	Thermo Fischer Scientific, Waltham, MA, USA	RRID:AB_2536183
donkey anti rat-Alexa 488	Thermo FischerScientific, Waltham, MA, USA	RRID:AB_2535794
Chemicals, peptides and recombinant proteins		
Ampuwa water	Ampuwa, Fresenius	40676.00.00
Aqua-PolyMount	Polysciences Inc.	18606
Bromophenol blue	AppliChem	A1120.005
Corn oil	Sigma-Aldrich	C8267-500ML
DNA Ladder 100bp	Thermo Fisher Scientific	15628019
DNA Ladder 1Kb Plus	Thermo Fisher Scientific	10787-018
dNTPs (100mM)	GE Healthcare	28-4065-52
EDTA	Merck	E6511
Ethidium bromide	Carl Roth	2218.2
Ethylene glycol	Merck	1009492500
Glacial acetic acid	Merck	A6283-1L
Glycerol	Sigma Aldrich	G5516
Hoechst 33258	Abcam	ab228550
Magnesium chloride ($MgCl_2$)	VWR	25108.260
Normal donkey serum (NDS)	Jackson ImmunoResearch	017-000-121
Paraformaldehyde (PFA)	Carl Roth	0335.2

(*Continued on next page*)

Continued

REAGENT or RESOURCE	SOURCE	IDENTIFIER
Potassium chloride (KCl)	VWR	26764.260
Potassium phosphate monobasic (KH_2PO_4)	Merck	P9791
RNase away	Roche	13398800
Sodium bicarbonate ($NaHCO_3$)	VWR	27775.293
Sodium chloride (NaCl)	VWR	27788.297
Sodium dihydrogen phosphate (NaH_2PO_4 $2H_2O$)	VWR	28013.264
Sodium hydroxide (NaOH)	VWR	31627.290
Sodium phosphate (Na_2HPO4)	VWR	28028.298
Sucrose	Sigma Aldrich	27480.360
Tamoxifen	Sigma Aldrich	T5648-5G
Taq DNA polymerase recombinant	Thermo Fischer Scientific	10342-020
Tissue Tek O.C.T.	Sakura	4583
Transcription Buffer (10x)	Roche	10881767001
Tris-HCl	Merck	108219.1000
Triton X-100	Merck	1.08219.1000
Tween-20	VWR	28829.183
Xylene cyanol	Sigma Aldrich	335940-10G
Bacterial and virus strains		
AAV1/2-EF1α-DIO-ChR2-eYFP	UKB Viral Core Facility, Bonn, DE	N/A
pAAV-EF1a-double floxed-hChR2(H134R)-mCherry-WPRE-HGHpA	Addgene, Watertown, MA, USA	20297-AAV1
AAV1/2-EF1α-pTRE-FLEX-ChETA-eYFP	UKB Viral Core Facility, Bonn, DE	N/A
AAV2/6-hSYN1-h-α- synuclein-WPRE	Sirion Biotech, Martinsried, Germany	Musgrove et al., 2019
Critical commercial assays		
RNAScope® Fluorescent Multiplex Detection Reagents	Advanced Cell Diagnostic	323110
Mm-Bcl11a-C3 RNA probe	Advanced Cell Diagnostic	N/A
Deposited data		
Imaging and quantitative data	Mendeley Data	Mendeley Data: https://doi.org/10.17632/4h9265nnrf.1
scRNaseq data	Fernandes et al., 2020	ArrayExpress: E-MTAB-9154
Experimental models: Cell lines		
KOLF-2 iPSC (human)	HipSci	RRID:CVCL_9S58
Experimental models: Organisms/strains		
Ai82D (TITL-GFP)	The Jackson Laboratory	RRID: MGI: J:219930
Bcl11a^{CreER}	Dr. Walid Khaled, University of Cambridge	Pensa et al., 2021
Bcl11a^{flox}	Dr. Pentao Liu, The University of Hong Kong; Prof. Stefan Britsch, University of Ulm;	RRID: J:194616
Bcl11a^{lacz}	Dr. Pentao Liu, The University of Hong Kong	RRID: J:219746
DAT$^{IRES-Cre}$	The Jackson Laboratory	RRID: MGI: J:114466
Dat^{tTA}	The Jackson Laboratory	RRID: MGI: J:218892
Oligonucleotides		
Primers for Ai82D, see Table S3	The Jackson Laboratory	N/A
Primers for Ai9, see Table S3	The Jackson Laboratory	N/A
Primers for Bcl11a-flox, see Table S3	This paper	N/A
Primers for Cre, see Table S3	The Jackson Laboratory	N/A

(*Continued on next page*)

Continued		
REAGENT or RESOURCE	SOURCE	IDENTIFIER
Primers for Cre-ER, see Table S3	The Jackson Laboratory	N/A
Primers for Dat-tTa, see Table S3	The Jackson Laboratory	N/A
Primers for LacZ, see Table S3	The Jackson Laboratory	N/A
Software and algorithms		
Affinity Designer 1.5.5	Serif, Notthingham, UK	https://affinity.serif.com/en-gb/ RRID: SCR_016952
Affinity Photo 1.5.5	Serif, Notthingham, UK	https://affinity.serif.com/en-gb/ RRID: SCR_016951
EthoVision XT version 9.0	Noldus, Wageningen, NL	https://www.noldus.com/ethovision-xt RRID: SCR_000441
Fiji version 1.0	Wayne Rasband, National Institute of Health, Bethesda, USA	https://imagej.net/RRID: RRID: SCR_002285
GraphPad Prism version 9.0	GraphPad	http://www.graphpad.com/scientific-software/prism/RRID/: SCR_002798
Metascape	Metascape	https://metascape.org/gp/index.html
R	The R Foundation of Statistical Computing, Vienna, AT	https://www.r-project.org/foundation/; RRID: SCR_000432
Stereo Investigator 9	MFB Biosciences, Williston, VTA, USA	https://www.mbfbioscience.com/stereo-investigator. RRID: SCR_002526
VisiView	Visitron Systems	https://www.visitron.de/products/visiviewr-software.html
ZEN blue software	Zeiss	https://www.zeiss.com/microscopy/int/products/microscope-software/zen.html, RRID:SCR_013672

RESOURCE AVAILABILITY

Lead contact

Further information and requests for resources and reagents should be directed to the Lead Contact, Sandra Blaess (sblaess@uni-bonn.de).

Materials availability

This study did not generate new unique reagents.

Data and code availability

- The accession number for the scRNA sequencing is ArrayExpress: E-MTAB-9154, as reported in Fernandes et al. (2020). Imaging and quantitative data have been deposited at Mendeley and are publicly available as of the date of publication. DOIs are listed in the Key resources table.
- This paper does not report original code.
- Any additional information required to reanalyze the data reported in this paper is available from the lead contact upon request.

EXPERIMENTAL MODEL AND SUBJECT DETAILS

Bcl11a^{lacZ} *mice* (Dias et al., 2016) were kindly provided by Pengtao Liu, School of Biomedical Sciences, The University of Hong Kong, China. *Bcl11a*^{flox} mice (Wiegreffe et al., 2015) were kindly provided by Pengtao Liu, School of Biomedical Sciences, The University of Hong Kong, China; and Neal Copeland, Institute for Academic Medicine, Houston Methodist and obtained from Stefan Britsch, University of Ulm. *Bcl11a*^{CreER} mice (Pensa et al., 2021) were kindly provided by Walid Khaled, Department of Pharmacology, University of Cambridge. *Bcl11a* cko mice were generated by crossing *Dat*$^{IRES\text{-}Cre}$ mice (Bäckman et al., 2006) with *Bcl11a*^{flox} mice (Genotype: *Dat*$^{RES\text{-}Cre/+}$, *Bcl11a*$^{flox/flox}$). In a subset of *Bcl11a* cko mice, the *Bcl11a*^{lacZ} null allele was introduced by crossing *Dat*$^{IRES\text{-}Cre}$ mice with *Bcl11a*$^{flox/lacZ}$ *mice* (Genotype: *Dat*$^{IRES\text{-}Cre/+}$, *Bcl11a*$^{flox/lacZ}$). Intersectional fate mapping experiments were performed by crossing

Bcl11a^{CreER} mice with the *Dat*^{tTA} (tetracycline trans-activator driven by the *Dat* promoter) mouse line (Chen et al., 2015) and the intersectional reporter mouse line Ai82D (Ai82(TITL-GFP)-D (Madisen et al., 2015) (Genotype: *Bcl11a*$^{CreER/+}$, *Dat*$^{tTA/+}$, *Ai82D*$^{TITL\text{-}GFP/+}$). For viral tracings, *Bcl11a*$^{CreER/+}$ or *Bcl11a*$^{CreER/+}$, *Dat*$^{tTA/+}$ (intersectional) were used. Mice were kept on a mixed C57BL6/CD1 background. Developmental stages are indicated in the Results and Figure legends or in the methods section (for behavioral analysis and α-synuclein overexpression experiments). Mice were group housed in a controlled environment, with 12 hr light/night cycles and *ad libitum* availability of food and water. Day of vaginal plug was recorded as E0.5. All experiments were performed in strict accordance with the regulations for the welfare of animals issued by the Federal Government of Germany, European Union legislation and the regulations of the University of Bonn. The protocol was approved by the Landesamt für Natur, Umwelt und Verbraucherschutz Nordrhein-Westfalen (Permit Number: 84-02.04.2014.A410, 84-02.04.2016.A238 and 84-12.04.2015.A550). Both female and male mice were used for multiplex RNA *in situ* analysis, immunostaining, viral tracing experiments and α-synuclein overexpression. Male mice were used for behavioral experiments. For comparison of *Bcl11a* cko and control mice, littermates were used (from several litters).

Tamoxifen administration

Tamoxifen was administered by oral gavage to pregnant dams at E15.5 (0.05 ml/10 g body weight) or to adult mice (0.075 ml/10 g body weight) to label *Bcl11a*-expressing neurons. Tamoxifen (Sigma Aldrich) was prepared as a 20 mg/mL solution in corn oil (Sigma Aldrich).

Tissue processing

Pregnant females were sacrificed by cervical dislocation. Embryos were transferred into ice cold PBS, decapitated and dissected. P0 pups were decapitated, and their brain dissected in ice cold PBS. Heads (E12.5 – E15.5) or brains (P0) were fixed in 4% paraformaldehyde (PFA) overnight at 4°C. Adult mice were anesthetized with an intraperitoneal injection of Ketanest/Rampun or pentobarbital and subsequently perfused transcardially with phosphate buffered saline (PBS), followed by 4% PFA. The tissue was cryopreserved in OCT Tissue Tek (Sakura). Embryonic and P0 tissue was cryosectioned at 14 μm thickness and collected on glass slides, adult brains were cryosectioned at 40 μm thickness and free-floating sections were collected in anti-freeze solution.

For immunofluorescent staining, sections were re-fixed in 4% PFA for 10 min at room temperature (RT) and incubated in 10% NDS in PBS plus 0.2% Triton X-100 (Sigma-Aldrich) (0.2% PBT, used for embryonic and P0 tissue) or in 10% NDS in 0.5% PBT (adult tissue) for 1 hr at RT. Sections were incubated with primary antibody overnight at 4°C in 3% NDS in 0.2% PBT (embryonic and P0 tissue) or in 3% NDS in 0.3% PBT (adult tissue). For staining with the guinea pig anti-BCL11A antibody and in some cases for rabbit anti-TH antibody sections were incubated in the primary antibody for 72 hr at RT (guinea pig anti-BCL11A) or at 4°C (rabbit anti-TH antibody). Sections were washed 3 times for 5-10 min in 0.2% PBT (embryonic and P0 tissue) or in 0.3% PBT (adult tissue) and incubated for 2 hr at RT in secondary antibody in 3% NDS in 0.2% PBT (embryonic and P0 tissue) or in 3% NDS in 0.3% PBT (adult tissue). Sections were washed 3 times for 5-10 min in 0.2% PBT (embryonic and P0 tissue) or in 0.3% PBT (adult tissue) and mounted with Aqua Polymount (Polysciences Inc.). For the detection of BCL11A, biotinylated donkey anti-guinea pig antibody followed by Cy3-Streptavidin was used.

Processing of tissue from mice overexpressing α-synuclein involved post-fixation with 4% PFA for 24 hr followed by cryopreservation in 30% sucrose solution. Sections were cut at 35 μm thickness using a freezing microtome. Staining of these sections followed previously described protocols (Helwig et al., 2016). A list of primary and secondary antibodies is provided in Key resources table. The following primary antibody dilutions were used: 1:500 to 1:1000 for rabbit anti-TH, 1:500 for mouse anti-TH and rabbit anti-SOX6, 1:1000 for rabbit anti-ALDH1A1 and rabbit anti-RFP, 1:2000 for goat anti-β-gal and rat anti-GFP, 1:2500 for guinea pig anti-BCL11A, 1:5000 for rabbit anti-Calbindin and 1:20.000 for mouse anti-human α-synuclein. Biontinylated donkey anti-guinea pig antibody was used at a 1:200 dilution and Cy3-streptavidin at a 1:1000 dilution. Cy3-conjugated anti-goat Cy3 and all Alexa fluorophore-conjugated secondary antibodies were used at a 1:500 dilution.

Multiplex fluorescent *in situ* hybridization

Multiplex fluorescent RNA *in situ* hybridization on frozen sections from P0 and adult mice was performed using RNAscope Fluorescent Multiplex Detection Reagents (323110, ACDBio, Newark, CA, USA) according to the instructions provided by the manufacturer for frozen tissue (User Manual: 323100-USM). Hybridized probe was detected with TSA Plus Cyanine 3 (NEL760001KT, Perkin Elmer, Waltham, MA, USA). The probe for *Bcl11a* was designed by ACDBio (Cat No. 563701-C3). Sections were counterstained with TH and Hoechst, then mounted with Aqua Polymount (Polysciences Inc., Warrington, PA, USA).

Stereotactic viral vector injection

Viral tracing

Bcl11a^{CreER} and *Bcl11a*^{CreER}, *Dat*^{tTa} mice (4-20 weeks old) were anesthetized with Fentanyl/Midazolam/Medetomidin and placed into a stereotaxic apparatus. 1 μL of virus solution with a titer of Titer $\geq 1 \times 10^{13}$ vg/mL (AAV1/2-EF1α-pTRE-FLEX-ChETA-eYFP or AAV1/2-EF1α-DIO-ChR2-eYFP (both from UKB viral core facility, Bonn, DE) or AAV1/2-EF1α-DIO-ChR2-mCherry (Addgene, Watertown, MA, USA)) was injected unilaterally into the SNc (from Bregma: anteroposterior (AP), −2.3 mm; mediolateral (ML), −1.1 mm; dorsoventral (DV), −4.1 mm) or into the VTA (from Bregma: AP, −3.44 mm; ML, −0.48 mm; DV, −4.4mm). A 34 g beveled needle (WPI)

and a microinjection pump (WPI) were used to control the injection speed (100 nl/min). After the injection, the syringe was kept in place for 3 min and slowly retracted over 1 min. 8 days after viral injections Tamoxifen was administered to the mice by oral gavage (0.075 ml/10 body weight) for 3 consecutive days. Two weeks after the last Tamoxifen administration, mice were perfused.

Alpha-Synuclein overexpression

Recombinant adeno-associated viral particles (serotype 2 genome and serotype 6 capsid) were used to express human α-synuclein in the mouse substantia nigra. Gene expression was controlled by the human Synapsin 1 promoter and enhanced using a woodchuck hepatitis virus post-transcriptional regulatory element and a polyA signal downstream to the α-synuclein sequence. AAV-vector production, purification, concentration, and titration were performed by Sirion Biotech (Martinsried, Germany). Mice (5-8 months for comparison between *Bcl11a* cko^{flox} and control mice; 5-16 months for comparison between *Bcl11a* cko^{lacZ} and *Bcl11a-lacZ* mice) were treated with a single 1.5 μl injection of 4.0x10^{12} genome copies/ml using a stereotaxic frame with a mouse adaptor (Stoelting, Wood Dale, IL, USA) under isoflurane anesthesia. Stereotaxic coordinates were 2.3 mm posterior and 1.1 mm lateral to bregma; injection depth was 4.1 mm relative to dura mater. The injection was made at a rate of 0.4 μl/min using a Hamilton syringe fitted to a glass capillary. The capillary was left in position for an additional 5 mins before being retracted. A list of AAVs is provided in Key resources table.

Image acquisition

Images of fluorescently stained images were acquired at an inverted Zeiss AxioObserver Z1 equipped with structured illumination (ApoTome) and a Zeiss AxioCam MRm (Carl Zeiss, Oberkochen, DE). At 10X (EC PlnN 10x/0.3, Carl Zeiss, Oberkochen, DE) magnification, tile images were acquired with conventional epifluorescence. At 20X (EC PlnN 20x/0.5, Carl Zeiss, Oberkochen, DE), 40X (Pln Apo 40x/1.3 Oil, Carl Zeiss, Oberkochen, DE) and 63X (Pln Apo 63x/1.4 Oil, Carl Zeiss, Oberkochen, DE) magnifications, structured illumination was used to acquire tile images and z stacks. Some of the images taken with the 20X objective and all the images taken with the 40X and 63X objective are maximum intensity projections of z stacks. Tile images were stitched with Zen blue software (Zeiss, 2012).

Brightfield images were visualized with a Zeiss Axio Scope.A1 microscope, collected using AxioCam 503 Color and processed with Zen blue software (Zen lite, 2019).

In situ hybridized sections at adult stages were imaged at an inverted Zeiss AxioObserver equipped with a CSU-W1 Confocal scanner unit (50 μm pinhole disk, Yokogawa, Tokyo, JP). At 40X (C-Apochromat, 40x/1.2 water, Zeiss) magnification, tile images and z stacks were acquired with laser lines 405 nm, 488 nm and 561 nm. Images taken with the 40X objective are maximum intensity projections of z stacks. Tile images were stitched with VisiView software (Visitron Systems, Puchheim, DE).

Quantification of cell numbers

TH$^+$ β-gal$^+$ neurons and additional subset markers

The percentage of *Bcl11a*-expressing mDA neurons in SN or VTA at P0 and P30 was determined by quantifying TH$^+$ β-gal$^+$ neurons at four (P0) or three (P30) rostrocaudal midbrain levels (Franklin and Paxinos, 2007). TH$^+$ β-gal$^+$ neurons in CLi and RRF in the adult brain were analyzed separately from neurons in the SN or VTA. The number of TH$^+$ β-gal$^+$ neurons was counted unilaterally in the SN, VTA, RRF and CLi and normalized for the total number of mDA neurons per region separately. The analysis was performed on n = 5 *Bcl11a-lacZ* control mice and n = 5 *Bcl11a* cko^{lacZ} mice at P0, and on n = 6 *Bcl11a-lacZ* (control) mice and n = 6 *Bcl11a* cko^{lacZ} mice at P30. The percentage of *Bcl11a*-expressing mDA neurons co-expressing additional subtype markers (SOX6 and CALB1 at P0; CALB1 and ALDH1A1 at P30) in SN or VTA was determined by quantifying TH$^+$ β-gal$^+$ neurons at four rostrocaudal midbrain levels (Franklin and Paxinos, 2007). The number of TH$^+$ β-gal$^+$ neurons co-expressing the respective subset marker in these regions was counted unilaterally and the numbers were normalized for the total number of TH$^+$ β-gal$^+$ mDA neurons in each region (SN or VTA). This analysis was performed for n = 5 *Bcl11a-lacZ* mice and n = 5 *Bcl11a* cko^{lacZ} mice at P0 and for n = 3 *Bcl11a-lacZ* mice and n = 3 *Bcl11a* cko^{lacZ} mice at P30.

Stereology

Analyses were performed on SNc samples by an investigator blinded to the sample codes. Unbiased stereological estimates of the number of nigral neurons were obtained by counting under brightfield or confocal microscopy. Samplings were performed on every fifth section throughout the entire SNc. Delineations were made using a 4x objective, and counting was performed using a 63x Plan-Apo oil objective (Numerical aperture = 1.4). A guard zone thickness of 1 μm was set at the top and bottom of each section. Cells were counted using the optical fractionator technique (Stereo Investigator software version 9, MBF Biosciences, Williston, VTA, USA) using a motorized Olympus microscope (IX2 UCB) equipped with an Olympus disk spinning unit (DSU) and a light sensitive EM-CCD camera. Coefficient of error was calculated according to (Gundersen and Jensen, 1987); values < 0.10 were accepted.

Analysis of fiber density

TH-expressing fibers

40 μm sections of 3 to 6 rostrocaudal levels of the striatum were stained for TH and epifluorescence images were taken using and inverted Z1 Axioobserver microscope with 10X objective. The mean gray value of the TH$^+$ striatal projections was calculated in the dorsal striatum, OT and TS (divided into ventral and dorsal TS) with Fiji/ImageJ and normalized for background fluorescence (corpus

callosum which is devoid of TH^+ fibers or neurons). This analysis was performed for n = 3 control mice and n = 3 Bcl11a cko^{lacZ} mice at P30.

EGFP-expressing fibers (intersectional genetic labeling)

40 μm sections of 5 rostrocaudal levels of the striatum were stained for TH and EFGP and epifluorescence images were taken using an inverted Z1 Axioobserver microscope with 10X objective. The mean gray value of the $EGFP^+$ projections was calculated in the OT, NAc (divided into core and shell of the NAc), the rostral striatum (RS), DS (divided into medial and lateral DS) and TS (divided into ventral and dorsal TS) with Fiji/ImageJ and normalized for background fluorescence (cortex which is devoid of $EGFP^+$ fibers). More specifically, $EGFP^+$ fibers in the OT were analyzed at Bregma 1.42mm, 0.95mm, 0.62 mm and −0.15 mm. For the analysis of $EGFP^+$ projections to the NAc core and shell and the RS, the mean gray value was calculated at Bregma 0.95mm and 1.42mm, respectively. $EGFP^+$ fibers in the medial and lateral DS were analyzed at Bregma 0.62 mm and −0.15 mm, while those in the dorsal and ventral TS were analyzed at Bregma −0.58mm. The analysis was performed for 7 mice at P30.

EGFP-expressing fibers (stereotactic viral vector injections)

40 μm sections from one to three rostrocaudal levels of the striatum per animal were stained for TH and EFGP and epifluorescence images were taken using and inverted Z1 Axioobserver microscope with 10X objective. The mean gray value of the $EGFP^+$ projections was calculated in the OT (devided into medial and lateral OT) and NAc (divided into core and shell of the NAc) with Fiji/ImageJ. Subsequently, the background fluorescence (cortex which is devoid of $EGFP^+$ fibers) was subtracted and the obtained value normalized for the average gray value of the analyzed areas to account for differences in recombination efficiencies between animals. This analysis was performed for 6 mice.

Behavioral tests

Male mice were kept *ad libitum* in groups of 2-3 animals in a 12-hour day/night rhythm on a normal diet. Animals ranging from two to four months of age were transferred to the examination room for experimental purposes and each one was housed in a separate cage. After a one-week acclimatization period in the examination room, mice performed the rotarod test and beam walking assay (both tests in one day) for five consecutive days, followed by a social recognition test (data not shown) and finally by the open-field test. All behavioral tests were performed with the experimenter being blinded to the genotype of the mice.

RotaRod

The animals were taken out of the cage and were acclimated to the rotarod apparatus (Ugo Basile, Gemonio, IT; Code no. 47600) in a 5-minute run on a rod rotating at a constant speed of 8 rpm. Afterward the animals went through three test runs per day, with a break of 30 min between each run. In each test run, the animals had to balance on the rotating rod for 5 min, whereby the torque increased from 4 to 40 rpm within 5 min. The duration that each mouse was able to stay on the rotating rod in each trial was recorded as the latency to fall. The three test runs per day were repeated on 5 consecutive days. During the test, the rod was kept clean and dry by wiping the mouse urine and feces off.

Beam Walking Assay

To examine fine motor skills independent of rotational movement (Luong et al., 2011), the beam walking assay (balanced beam test) was used (Carter et al., 1999). Animals had to balance from one platform over a 12 mm wide and 1 m long rod made of synthetic material to another platform that held a box with a food reward. Beams were placed 50 cm above the table. The time taken for the animals to cross the bar was measured. If animals did not reach the safety platform or took longer than 60 s to cross the beam, a maximum of 60 s was assigned. The test was run for a period of 5 consecutive days.

Open-field test

In the open-field test, the mice were placed in an open arena (30 × 30 × 30 cm). They were allowed to move freely for 5 minutes. The animals were recorded by Video (EthovisionXT, Noldus, Wageningen, NL) and the running distance, the time spent in the border area, the corners and the center of the cage as well as crossings from the border to the center area were measured. This test was initially run for a training period of 1 day, then after a 30-day rest period another test run was performed. This test was run twice with a 30-day rest period in between. Since both runs showed comparable results, the results were combined for the final analysis.

Single cell RNA-sequencing

Processing, QC and normalization

The single-cell dataset used with the same processing QC and cell type annotation as described in Fernandes et al. (2020).

BCL11A Expression Visualization

To show *BCL11A* single cell expression on the uniform manifold approximation and projection (UMAP), *BCL11A* transcript counts were normalized by their cell's total detected transcripts, scaled to 10000 reads/cell and then log-normalized. For the barplots the *BCL11A* transcripts for every single-cell were transformed to counts per million. The error bars correspond to the variation observed within the cell type including dropouts.

BCL11A DAn1 transcriptomic signature and gene set enrichment analysis

To define genes that are related to *BCL11A* expression we split the DAn1 cells into two groups: *BCL11A*+ cells with at least 1 transcript and *BCL11A*- cells, with no detected transcripts. To identify differentially expressed genes we removed the *BCL11A* expression values from the transcriptome, since this was the main criterion of separation, and used scanpy (Wolf et al., 2018) to perform the

wilcoxon rank sum test between the two groups. For gene set enrichment analysis, we used Metascape (Zhou et al., 2019) considering the first 100 upregulated differential expressed genes shorted by according to their statistical test p value.

Neuronal vulnerability in BCL11A+ DAn1 neurons

To assess how relevant *BCL11A* expression is to neuronal vulnerability we examined two events in every DAn1 neuron: a) whether it is annotated as sensitive to rotenone treatment as described in (Fernandes et al., 2020) and b) whether BCL11A is detectable. We examined the relation of those two events using the Fisher's Exact test on the whole DAn1 population.

STATISTICAL ANALYSIS

Statistical analyses of cell numbers were performed with GraphPad Prism (9.0) software using unpaired t test and Welch's t test when comparing two groups and one-way ANOVA followed by test for linear trend, one-way ANOVA followed by Tukey's or Šídák's multiple comparison test or Welch's ANOVA followed by Dunnett's T3 multiple comparison test when comparing multiple groups. Welch′s t test and Welch′s ANOVA were performed for groups of data that were sampled from Gaussian populations, but did not have the same standard deviation. Statistical analyses of behavioral experiments were done with R studio. Open field tests were evaluated by one-way analysis followed by Tukey's post hoc test for multiple comparisons. Differences in the balanced beam test and rotarod were assessed by two-way ANOVA taking time and genotype as numerical and categorical variables. Sampls size estimation was not performed. For comparison between controls and *Bcl11a* cko animals, animals were assigned to experimental groups according to genotypes. No data or subjects were excluded from the analysis, except for experiments involving stereotactical injections. In this case, subjects were excluded if expression of the protein after viral transduction was not detected in the targeted region (SNc or VTA). Statistical details are described in the Figure legends, the Results or in the STAR method section (for single cell RNA-sequencing). P values of less than 0.05 were considered statistically significant. Data are reported as mean values ± standard error of the mean (SEM).